

1 **Large-scale, high-density (up to 512 channels) recording of local circuits in behaving**
2 **animals**

3
4 Antal Berényi^{1,2,3}, Zoltán Somogyvári^{2,4}, Anett J. Nagy³, Lisa Roux¹, John Long¹,
5 Shigeyoshi Fujisawa^{1,2,5}, Eran Stark¹, Anthony Leonardo⁶, Timothy D. Harris⁶ and György
6 Buzsáki^{1,2,6}

7
8 ¹The Neuroscience Institute New York University, School of Medicine, New York,
9 NY 10016, USA

10 ²Center for Molecular and Behavioral Neuroscience, Rutgers, The State University of
11 New Jersey, Newark, NJ 07102

12 ³MTA-SZTE ‘Momentum’ Oscillatory Neural Networks Research Group, University
13 of Szeged, Department of Physiology, Szeged, H-6720, Hungary

14 ⁴Wigner Research Center for Physics of the Hungarian Academy of Sciences
15 Department of Theory, Budapest, H-1121, Hungary

16 ⁵Laboratory for Systems Neurophysiology, RIKEN Brain Science Institute, Wako, Saitama,
17 351-0198, Japan

18 ⁶Howard Hughes Medical, Institute, Janelia Farm Research Campus, Ashburn, Virginia
19 20147, USA

20
21 Correspondence:

22 György Buzsáki

23 gyorgy.buzsaki@nyumc.org

24 NYU Neuroscience Institute, New York University, Langone Medical Center

25 East River Science Park, 450 East 29th Street, 9th Floor,

26 New York, NY 10016

27
28 **Running Head**

29 512 channel neuronal recording in behaving rodents

30

31 **Abstract**

32 **Monitoring representative fractions of neurons from multiple brain circuits in**
33 **behaving animals is necessary for understanding neuronal computation. Here we**
34 **describe a system that allows high channel count recordings from a small volume of**
35 **neuronal tissue using a lightweight signal multiplexing head-stage that permits free**
36 **behavior of small rodents. The system integrates multi-shank, high-density recording**
37 **silicon probes, ultra-flexible interconnects and a miniaturized microdrive. These**
38 **improvements allowed for simultaneous recordings of local field potentials and unit**
39 **activity from hundreds of sites without confining free movements of the animal. The**
40 **advantages of large-scale recordings are illustrated by determining the electro-**
41 **anatomical boundaries of layers and regions in the hippocampus and neocortex and**
42 **constructing a circuit diagram of functional connections among neurons in real**
43 **anatomical space. These methods will allow the investigation of circuit operations and**
44 **behavior-dependent inter-regional interactions for testing hypotheses of neural**
45 **networks and brain function.**

46

47 **Keywords:**

- 48 - Local field potential
- 49 - Unit firing
- 50 - monosynaptic connections
- 51 - behaving rats and mice

52

53

54 **INTRODUCTION**

55 While the exploration of the wiring diagram of brain networks is moving forward at an
56 unprecedented scale (Lichtman and Denk 2011) and steady innovations in optogenetics
57 provide a toolset for identification and manipulation of circuit components (Boyden et al.
58 2005; Lein et al. 2007; Madisen et al. 2012; Prakash et al. 2012; Tye and Deisseroth 2012;
59 Yizhar et al. 2011), complementary methods for monitoring the activity of large numbers of
60 neurons in multiple local circuits in the behaving animal are lagging (Alivisatos et al. 2013;
61 Buzsaki 2004; Nicolelis et al. 1997). Yet, monitoring a statistically representative fraction
62 of neurons of the investigated circuits in behaving animals is a prerequisite for
63 understanding neuronal computation (Alivisatos et al. 2013; Alivisatos et al. 2012; Buzsaki
64 2004; Carandini 2012; Nicolelis et al. 1997). Currently, recordings of individual neurons
65 and local field potentials (LFP) in local circuits at high temporal resolution are possible
66 with wire or nano-machined microelectrodes ('silicon probes') (Blanche et al. 2005;
67 Buzsaki 2004; Du et al. 2011; Wilson and McNaughton 1993) (Buzsaki et al. 2012;
68 Logothetis 2003). High-density probes can record from multiple cortical and subcortical
69 structures in the freely behaving animal at the spatial resolution of single neurons (Blanche
70 et al. 2005; Buzsaki 2004; Csicsvari et al. 2003; Du et al. 2011; Fujisawa et al. 2008;
71 Montgomery et al. 2008). Furthermore, silicon probe recordings can be combined with
72 optogenetic methods for the identification of neuron types and selective manipulation of
73 local circuits (Anikeeva et al. 2012; Boyden et al. 2005; Royer et al. 2010; Stark et al.
74 2012).

75

76 While silicon probe technology is poised to offer ever-larger site numbers and smaller
77 volume probes (Du et al. 2011; Du et al. 2009), significant improvements and
78 miniaturization are needed at the level of head-stage interconnects, signal multiplexing,
79 ultra-flexible connection between the animal and the recording equipment, and signal
80 processing (Du et al. 2011; Szuts et al. 2011; Vandecasteele et al. 2012). One critical aspect
81 of miniaturization is the deployment of signal multiplexers. Previously used multiplexers
82 have either low channel counts or limited high- or low-pass frequency characteristics for
83 simultaneous recordings of both unit and LFP signals in the physiological range (Du et al.

84 2011; Harrison 2008; Olsson et al. 2005; Szuts et al. 2011; Viventi et al. 2011). Below, we
85 present the development of a high throughput integrated microelectronic system, including
86 high-density, multiple-shank recordings of unit activity and LFP from multiple brain
87 regions, using on-stage signal multiplexing methods. Applications are demonstrated in
88 freely moving rats and mice, including extension to optogenetic manipulations.

89

90 **MATERIALS AND METHODS**

91 *Animal surgery, recording, and behavioral paradigms.* All experiments were approved by
92 the institutional Animal Care and Use Committee of New York University Medical Center,
93 and the Ethical Committee for Animal Research at the Albert Szent-Györgyi Medical and
94 Pharmaceutical Center of the University of Szeged. The experiment protocol was in
95 agreement with the European Communities Council Directive of November 24, 1986
96 (86/609 ECC) and the National Institutes of Health Guidelines for the Care and Use of
97 Animals for Experimental Procedures. Five male Long-Evans rats (400–640 g; 3 to 10
98 months old) were implanted with high-density, 256-site silicon probes under isoflurane
99 anesthesia, as described earlier (Vandecasteele et al. 2012). The probes and the polyimide
100 interconnect cable were manufactured by NeuroNexus, Inc. (<http://www.neuronexus.com>).
101 In two rats, two probes were implanted; in one rat the probes were placed in the same
102 hemisphere, whereas in the other animal they were placed symmetrically in the two
103 hemispheres (Fig. 1). During surgery, the tips of the shanks are inserted into the superficial
104 cortical layers or approximately 1 mm above the intended subcortical target. After
105 recovery, the probe is moved gradually until the target layer is reached, using 70 to 150 μ m
106 rotations per day are made until most or all shanks record units and the probe has reached
107 the desired target. The operated animals were housed in individual cages.

108

109 Neuronal activity in the neocortex and/or the hippocampus was recorded while the animals
110 were running in a 240-cm long linear maze or were performing a delayed alternation task in
111 a similar size T-maze for water reward, or were freely exploring an open field platform.
112 The neuronal activity during rest/sleep in the home cage, preceding and following the
113 waking sessions were also recorded. The wide-band signal was low-pass filtered and down

114 sampled to 1250 Hz to generate the local field potential (LFP) and was high-pass filtered
115 (>0.8 kHz) for spike detection. Malfunctioning recording sites (due to high impedance,
116 cross-talk, short circuit) were removed from the analysis. Operated mice (male, 8-20
117 weeks) were also housed individually after surgery. Details of surgery, optogenetical
118 methods and behavioral tests are available in Stark et al. (2012) (Stark et al. 2012).

119

120 *Histology.* Following the termination of the experiments, the animals were deeply
121 anesthetized, and transcardially perfused first with 0.9% saline solution followed by 4%
122 formaldehyde solution. The brains were sectioned by a Vibratome (Leica, Germany) at 100
123 μm , parallel with the plane of the implanted silicon probes. Sections were DAPI stained and
124 mounted in Fluomount (both Sigma-Aldrich, USA). Some sections were immunostained
125 against calbindin to determine the border between CA3 and CA2. The tracks were typically
126 reconstructed from a few adjacent sections.

127

128 *Single unit analyses.* Extracellular representations of action potentials were extracted from
129 the recorded broad-band signal after high pass filtering (>800 Hz) by a threshold crossing-
130 based algorithm. The dimensionality of the spike waveform representations on 32 contact
131 sites of a given shank were reduced using principal component analysis, and the individual
132 spikes were automatically clustered into groups with the possible lowest internal variance
133 (i.e. representing action potentials generated by single neurons) using KlustaKwik (Harris
134 et al. 2000). The generated cluster groups were manually refined by discarding multiunit
135 clusters showing corrupted autocorrelograms. Groups with unstable firing patterns over
136 time were also deleted. To compare the quality of single unit cluster isolation under various
137 conditions, cluster qualities were estimated using the following two conjunctive measures
138 (Harris et al. 2000; Stark et al. 2012). (1) Cluster overlap in the high dimensional feature
139 space was estimated by the Mahalanobis distance (isolation distance, ID). (2) The ratio
140 between the frequency of spikes present within 0-2 ms interspike interval and those at 0-20
141 ms interval was defined as the interspike-interval ratio (ISI ratio), and used as a measure of
142 possible contamination of an isolated single unit by spikes of another unit. We used two
143 levels of criteria to exclude contaminated clusters from our analyses. In the ‘permissive’

144 approach, clusters with either ISI ratio < 0.4 OR ID > 30 were included, while in the
145 ‘conservative’ analyses clusters only with ISI ratio < 0.2 AND ID > 40 were included.

146 The number of simultaneously recorded units (unit-yield) were quantified as an average
147 number of neurons per session per recording site overlapping with cellular layers.

148 For behavior-related analyses, the spatial position of the animal was sampled every 30 ms,
149 with 3 mm resolution. For LFP phase-dependent circular metrics, the phase of each LFP
150 frequency component was determined by Hilbert-transforming the zero-phase shift digital
151 filtered LFP ($2 \times 4^{\text{th}}$ order Butterworth infinite impulse response filter).

152

153 *Cross-correlation analysis.* Monosynaptic interactions of single units were determined by
154 the examination of the cross-correlograms. Short-latency (1-5 ms), narrow (1-2 ms) peaks
155 or troughs (monosynaptic excitation or inhibition, respectively) were deemed significant if
156 they crossed a global threshold band determined from a surrogate dataset of 1000 jittered
157 spike trains (99% confidence interval, ± 0.4 ms jittering with uniform distribution;
158 (Fujisawa et al. 2008). For monosynaptic interaction-based network mapping (Fig. 11), the
159 permissive dataset of single units was used, since a moderate contamination of the unit
160 clusters does not introduce spurious short-latency peaks. Spike contamination increases
161 ‘noise’ in the cross-correlogram and, in fact, decreases the probability of finding
162 monosynaptically connected neuron pairs.

163

164 *Spike triggered LFP maps.* Sixty-ms long low-pass filtered (< 600 Hz) perispike LFP traces
165 centered at the spikes occurrences of the spike-train of selected neurons were extracted. The
166 LFP segments for each recording sites were high pass filtered (20 and 5 Hz for run and
167 sleep sessions, respectively; zero-phase shift $2 \times 4^{\text{th}}$ order Butterworth infinite impulse
168 response filter). The purpose of the higher cutoff frequency for run sessions was to
169 eliminate the large amplitude theta fluctuation. The filtered peri-spike segments were
170 averaged across multiple spikes (usually a few thousand occurrences for run sessions, and
171 few hundreds for sharp-wave ripple segments). The mean peri-spike LFPs of the 256 or 512
172 recording channels were reordered in 2D to match with the anatomical layout of the
173 recording sites on the silicon probe, forming an activity map of the recorded structures.

174 Consecutive data points in each segment were visualized as multiple frames of a movie,
175 using the following equation:

$$MAP_{ij} = \frac{\tan^{-1}\left(\frac{LFP_{ij}}{\max LFP} * zf\right)}{\tan^{-1}(zf)}, \quad i \in N\{1, \dots, 8\}, \quad j \in N\{1, \dots, 32\}$$

176 where MAP_{ij} is the transformed activity value of the i^{th} shank and j^{th} contact site to be
177 displayed, LFP_{ij} is the filtered mean LFP value of a given channel, and zf is an arbitrary
178 zooming factor. This transformation helped to visualize the smooth activity patterns while
179 relatively suppressing the gross changes. The generated activity-map (heatmap) frames
180 were further smoothed in space by cubic spline interpolation (10x upsampling), and in time
181 by a 150 μs (three sample) wide moving average filter. A schematic of the anatomical
182 layers was overlaid on each frame, based on the histological verification of electrode
183 location.

184

185 *Mapping high frequency power.* The LFP signals were filtered by a narrow gaussian band-
186 pass filter (peaks at 300 Hz, SD = 10 Hz) and the power was summed up for 1-second-long
187 periods. Several other high-passed signal bands (>300 Hz) provided similar results. In the
188 hippocampus, the selected periods typically contained a sharp wave ripple event to
189 maximize the presence of unit firing since the goal was to identify the somatic layers.
190 Several other frequency bands and bandwidths were tested and the 300 Hz band was found
191 empirically the most effective to outline the cell body layers (Ray and Maunsell 2011). This
192 band was also less sensitive than higher frequencies due to the wide amplitude range of the
193 isolated units that vary from site to site. The high frequency power distribution effectively
194 outlined the CA1 and CA3 pyramidal layers and the dentate area. In addition, the high
195 frequency power map agreed well with the locations of the clustered neurons. The predicted
196 positions of the cell body layers were in good agreement with the anatomically
197 reconstructed tracks of the probe shanks.

198

199 *Coherence analysis.* Using coherence as similarity measure, an interaction-energy based
200 clustering was implemented to identify cell layers. Every site served as a reference against

201 all the other referred sites. The resulting values were clustered using a gradient-descent
202 algorithm, so that each site was merged with that cluster for which the resulting coherence
203 gain after merging was the largest. Starting from random initial assignments, the clustering
204 algorithm formed stable but fewer clusters corresponding to a local energy minimum.
205 Energy of cluster A is defined as:

$$E^A = \frac{-1}{N^A} \sum_{i,j \in A} C_{ij}$$

206 Where, C_{ij} is the coherence between i^{th} and j^{th} sites and N^A is the number of recording sites
207 in cluster A. The energy gap between two different assignments to cluster A and B of site i
208 is:

$$E^A = \frac{-1}{N^A} \sum_{i,j \in A} C_{ij}$$

209 If the energy gap is positive, site i is moved into cluster B, otherwise it remains in cluster
210 A. Since the method results only local minima of energy and stochastic components, such
211 as the random initial condition and update order affects, clustering consistency was verified
212 by repeating the process several times. Small (less than 3 sites in a cluster) and scattered
213 clusters (typically representing bad channels) were deleted and their sites were included
214 into the majority cluster of their immediate neighborhood. This clarification was done
215 either before and after merging the coherence clusters and MUA map. The resulting
216 clusters effectively differentiated the different anatomical layers of the hippocampus (Fig.
217 5). The same coherence similarity method was used in the neocortex to differentiate the
218 superficial, middle (layer IV) and deep layers of the neocortex (Fig. 8).

219

220 *Merging the MUA and coherence cluster maps.* MUA map was thresholded at 70% of its
221 maximum to define the cellular layers (CA1 and CA3 pyramidal and DG granular). These
222 sites were deleted from the coherence clusters to define new clusters. As a result, the CA1
223 and CA3 pyramidal layer and the granular layer became different clusters, designated as
224 cell body layer clusters.

225

226 *Coastline display.* In a different display, each site was connected to the most coherent sites

227 on the neighboring shanks, which connected forward to the most coherent site of the next
228 shank, and so on. The recording positions were slightly and randomly scattered, to assist
229 visualizing the different lines crossing the same points. The connecting lines were colored
230 on the basis of the cluster identity of their seed.

231

232 *Estimation of recording quality and comparison to a commercially available non-*
233 *multiplexing recording system.* In order to obtain an objective measure of the recording
234 quality of our multiplexing system, we performed the following analyses. The input-
235 referred noise of the recording channels was measured by short circuiting all inputs of the
236 INTAN chip to the reference channel. The power spectrum of a ten second-long recording
237 was whitened after performing Fourier transformation. To evaluate the quality of recorded
238 LFP and units, several consecutive, ten-minute long sessions (typically during immobility
239 and sleep) were recorded from the hippocampus with a Buzsaki32 four-shank silicon probe
240 (NeuroNexus Inc.). The recordings were made with either our multiplexed system (test) or
241 a commercially available non-multiplexed system (control) in an alternating sequence. The
242 control system consisted of a headstage (gain=20x; HST/32V-G20; Plexon Inc, Dallas, TX,
243 USA), connected by a 40-wire Litz cable (same length as in the multiplexer's cable) to a
244 Digital Lynx 16SX A/D converter (Neuralynx, Bozeman, MT, USA). The multiplexed
245 signals were sampled at 20 kS/s, while the Digital Lynx used 32 kS/s sampling. Pearson's
246 linear correlation was calculated across all combination of channels (496 pairs), and
247 visualized as a correlation matrix. A mean correlation value of the entire 10-minute long
248 recording was calculated for channels on the same shank (within-shank correlation), and for
249 channels located on different shanks (across-shank correlation). To estimate the
250 contribution of higher frequency components in the correlation, we repeated the analysis
251 twice after passing the signals through a low-pass 4th order Butterworth zero-phase lag
252 digital filter (arbitrarily chosen 10 Hz and 100 Hz cutoff frequencies, respectively). The
253 raw recorded signals were processed to extract single unit spike trains, and clustered
254 automatically by the KlustaKwik program (Harris et al. 2000). To avoid subjectivity, the
255 manual cluster refinement step was limited to eliminate the obvious noise clusters
256 (waveforms with same amplitude and shape on every recording sites of the given shank).

257 The number and quality of the isolated single units were assessed using the following three
258 criteria. In the first analysis, the number of automatically isolated non-noise clusters were
259 compared, disregarding their isolation quality. In the second comparison, we measured the
260 ratio of the number of isolated spikes and the number of ‘noise’ waveforms to estimate the
261 signal to noise ratio. Third, we used two levels of cluster quality measures (‘permissive’
262 and ‘conservative’; see above). The recorded waveforms of identical spike clusters
263 recorded by the two systems were also compared after amplitude normalization, and offline
264 interpolation (upsampling) to 50 kS/s.

265

266 **RESULTS**

267 **System Description**

268 Large-scale recordings from multiple single units, large spatial coverage and limited tissue
269 displacement/damage by the electrodes are competing conditions (Buzsaki 2004; Du et al.
270 2011). Our goal was to monitor single unit and LFP activity patterns of neighboring
271 neocortical regions and interconnected hippocampal subregions. To this end, we designed
272 an 8-shank probe with 32 recording sites on each shank (Fig. 1A). The recording sites are
273 arranged vertically at 50- μm steps, providing sufficient spatial resolution for unit clustering
274 (Csicsvari et al. 2003; Montgomery et al. 2008; Wilson and McNaughton 1993), yet large
275 vertical coverage (1550 μm). Each recording site is 165 μm^2 and has an impedance
276 between 1.3 to 3 Mohms. The shanks are placed 300 μm apart to eliminate simultaneous
277 recording of neurons by adjacent shanks (Henze et al. 2000) and provide spatial coverage
278 of adjacent neocortical modules or hippocampal regions (Csicsvari et al. 2003). Each shank
279 is 15 μm thick, and tapered from a sharp tip to 96 μm at the uppermost recording site to
280 minimize tissue damage, yet rigid enough to allow smooth penetration through brain tissue.
281 The total volume of the probe shank, containing the recording sites, is comparable to a
282 traditional wire tetrodes (Wilson and McNaughton 1993). In contrast to the blunt tetrode,
283 which often tears intracortical blood vessels during penetration, the tapered profile of the
284 silicon probe shanks allows it to be moved up and down in the brain with continued yield of
285 units. The probe is connected to a microdrive so that the probe sites can be advanced to the
286 vicinity of the desired neurons (Vandecasteele et al. 2012) (Fig. 2).

287

288 *Signal multiplexing and processing*

289 A major challenge of the effective use of silicon probes in small animals is to reduce the
290 volume and weight of the instrumentation between the probe and the recording equipment.
291 Multiple connectors, traditional preamplifiers and multi-strand cables for each recording
292 site are not viable for high-density probes; the large volume and weight of these
293 components and the increased tension of the connecting cable significantly limit the
294 behavior of the small rodent. In addition, using large numbers of individual external
295 amplifiers is prohibitively costly and involves complex cabling. A logical solution to these
296 problems is the deployment of time-division multiplexing (Harrison 2008; Olsson et al.
297 2005; Szuts et al. 2011; Viventi et al. 2011). To this end, we used 32-channel VLSI analog
298 signal multiplexers developed specifically for brain recording applications (Harrison 2008)
299 (RHA2132, INTAN Inc., www.intantech.com). Eight multiplexers are soldered to a
300 custom-designed printed circuit board, four on each side (Fig. 1A), to transmit a total
301 number of 256 channels. To allow movement of the probe, and preserve its small inertia an
302 ultra-flexible polyimide-based cable was designed and served as an interconnect between
303 the probe and the multiplexing headstage (Fig. 1A).

304

305 Each of the 256 electrical signals acquired by the silicon probe is amplified and band-pass
306 filtered (gain = 200x, cutoff frequencies of the high-pass and low-pass filters are 0.3 Hz, -6
307 dB/octave and 10 kHz, -18 dB/octave, respectively) (Fig 1B). The broadly tuned cutoff
308 frequencies allow the recording of broad-band signals (LFP and unit activity
309 simultaneously) from all recording sites. The signal multiplexer chips were programmed to
310 switch sequentially between channels every 1.5 μ s, so that a sweep of 32 channels
311 corresponds to 48 μ s (Fig 1C, D). To accomplish a 50- μ s cycle length (20 complete scan
312 cycles in a millisecond), the last channel of the 32-channel block was transmitted for two
313 more microseconds before looping back to the first channel of the subsequent cycle. The
314 post-loop 2 μ s time was used to protect against desynchronization of the multiplexing
315 sequence. Potential desynchronization of the multiplexing and demultiplexing sequence
316 may occur if the clock signal accidentally advances the sequence of the multiplexed signal.

317 Such accidental ‘jumps’ are avoided by resetting the binary counters to zero (binary code
318 00000) during the 2- μ s post-loop time. This clock supervision mechanism ensured that
319 even if the clock code is corrupted for any reason, only one sample is misplaced in the
320 sequence of the parallel-decoded channels. To reduce the wiring complexity of the printed
321 circuit board interconnects, the 32 recording sites of a given shank did not correspond to a
322 single multiplexer but were distributed among at least four chips. This had the added value
323 that in case of a chip failure some recordings from all shanks remained available.

324

325 We found that the relatively high output impedance of the RHA-2132 multiplexer chip was
326 not sufficient to reliably transmit signals over long data cables (over 5 meters), typically
327 needed in behaving experiments. To improve signal settling time and to circumvent the
328 capacitive load of the cable, high precision operation amplifiers (MCP622; Microchip,
329 USA; slew rate: 27 V/ μ s; Fig. 3D) were added in series to buffer the multiplexed signals.
330 With the added buffering, the signal settled in less than 100 ns to 1% precision after each
331 switch of the multiplexer chip even when up to 15 meter-long cable, consisting of 36-gauge
332 (110 μ m) Litz wires, was used. The ultra-light and ultra-flexible cable allowed for a free
333 movement of the animal (Vandecasteele et al. 2012) (Fig. 2F).

334

335 To achieve synchronous channel advancement on every multiplexer chip without adding
336 further weight and surface area to the head stage, the common clock signal (640 kHz, 50%
337 duty cycle) is generated by a programmable integrated circuit in the external controller box
338 (‘main box’). A five-bit binary clock code was generated by a synchronous binary counter
339 (74HC163; Texas Instruments, USA) on the head stage to address the channels of the
340 multiplexers within blocks of 32. In the main box, the multiplexed signals were further
341 amplified (gain = 2, total gain = 400), and their baseline was corrected by the subtraction of
342 a preset DC value. The multiplexed signals (Fig. 1C, D) were sampled by a high-speed
343 digital-to-analog converter (PCI-6133; National Instruments, USA). Sampling was initiated
344 by the mainbox’s clock generator microchip 125 ns prior to the subsequent channel switch
345 to maximally exploit the available signal settling time.

346

347 *Software control*

348 To generate the clock and trigger signals, the programmable integrated circuit was activated
349 by the recording software only after the digital-analog data acquisition (daq) task was
350 properly set up, and was idle for the external trigger to start sampling. The recording
351 software program acquired samples from the buffer in chunks of 100 ms (100 ms x 20
352 samples per ms x 32 channel= 64000 samples per multiplexed line). This 100 ms (10 Hz)
353 readout frequency offered a practical compromise between minimizing the time
354 requirement introduced by the frequent updates of the processing code headers, yet
355 provided a smooth, real-time-like data display on the computer screen. After the buffer has
356 been filled, the acquired data was read out by the recording software and was reordered to a
357 32 x 2000 size matrix. The synchronous initiation of the sampling and clock advancement
358 ensured that the dataset of each buffer readout started with a sample corresponding to the
359 first channel on the input side of the multiplexer chip (Fig. 1D). Although the actual clock
360 code of the software and the hardware was not synchronized after the initiation, we never
361 experienced any misalignment of the channel order even after extended testing of the entire
362 system up to 40 kS/s sampling speed per channel. The electrophysiological recording setup
363 was combined with a universal serial bus (USB) web camera recording system for the
364 continuous monitoring of the animal's position and behavior (Figures 2 and 3).

365

366 *Real time hardware demultiplexing*

367 Many applications need not only recording of the neuronal signal but also its real time
368 availability, e.g., to interact with brain circuits in close-loop experiments (Berenyi et al.
369 2012; Stark et al. 2012). However, the content of the buffer of the analog-digital card is
370 read only once every 100 ms, and the software routines introduced between an analog-
371 digital and digital-analog conversion *per se* provide a suboptimal time precision for brain
372 feedback stimulation. To achieve real-time readout (<50 μ s per sample), we designed a
373 mixed analog/digital demultiplexing device (Fig. 4). The demultiplexer, in addition to
374 receiving analog data streams, was timed by the same clock signal that drove the head
375 stages, and the rest of the clock bits were generated by the principle as described above for
376 the multiplexers. Two separate bit-masks (two-bit and three-bit) were generated by a

377 microcontroller-driven user interface that allowed the selection of any one of the eight
378 multiplexed streams (using an analog switch circuit), and any of the desired channels of the
379 selected stream (one of 32). Demultiplexing was established by a pattern matching
380 algorithm: the real five-bit clock signal was compared to the user preset clock bit mask by a
381 series of XNOR and AND logic gates. The digital output of the circuit generated a digital
382 high level only if the clock mask matched the real clock signal (i.e., approximately the
383 duration of the desired channel's segment within the multiplexed stream). In principle, this
384 digital pulse was suitable to trigger the sampling mode (i.e., a voltage follower) of a
385 sample-and-hold integrated circuit, which worked as a voltage follower. The falling edge of
386 the trigger pulse switched the sample-and-hold circuit to hold the last voltage value until
387 the next sampling cycle, thus bridging the time gap while the consecutive channels were
388 transmitted in the multiplexer line (Fig. 4A). Because the propagation time of the digital
389 gates introduced a significant delay in the digital trigger pulse, it could not be used directly
390 to trigger the sample-and-hold circuit. To correct for the delay, a monostable multivibrator
391 ('one shot') was used to generate a shorter pulse (1.3 μ s) so that the sampling was
392 terminated before switching to the subsequent sample in the multiplexer line. The output of
393 the sample-and-hold circuit was then low-pass filtered (at 10 kHz) to eliminate the step
394 responses (Fig. 4B). The reconstructed analog signal was amplified or filtered further as
395 required for audio-monitoring the recorded signal or viewing the waveform on an
396 oscilloscope (0.5 Hz-5 kHz; Fig. 4D and E).

397

398 *Physical dimensions*

399 To eliminate complex cabling and connections of high-channel counts of the probe, the
400 probe was permanently connected to the 256-channel multiplexer headstage (4.7 grams; 34
401 mm x 39 mm x 2.5 mm) and is worn chronically by the rat. During recording, the animal
402 was connected to the recording system through an ultraflexible cable (Vandecasteele et al.
403 2012) (twelve 127 μ m diameter insulated copper wires, 455 μ m total diameter cable; Fig.
404 2F). For recording from smaller size silicon probes or tetrodes targeting multiple brain
405 structures, we constructed 32- and 64-channel versions of the multiplexer headstage (32
406 channel 0.9 gram; 13 mm x 15 mm x 3 mm; 64 channel: 1.2 gram; 13 mm x 19 mm x 3

407 mm, respectively; Fig. 3). In contrast to the 256-channel version, the front ends of these
408 headstages were connected to the probe output by high-density connectors (Omnetics, Inc.)
409 during the experiments.

410

411 *Validation of the recording system and estimation of the signal quality*

412 We estimated the mean input referred noise spectrum for all channels of the 32-channel
413 multiplexer headstage (the results presented here applies to the 64- and 256-channel
414 headstages as well, since they consists of parallel-connected 32-channel blocks). When the
415 input channels were short-circuited with the reference pin of the headstage, the mean RMS
416 amplitude of 60 Hz noise was 7.2 μV (range = 2 - 8.5 μV), which is approximately one
417 order of magnitude higher than the $\frac{1}{2}$ least significant bit of the A/D conversion. We also
418 compared the signal quality to a commercially available recording system (HST/32V-G20
419 pramplifier (Plexon Inc, Dallas, TX, USA) and Digital Lynx 16SX A/D converter
420 (NeuraLynx Inc, Bozeman, MT, USA). The amplitude of the signal was approximately
421 20% smaller using the INTAN amplifier chips than that of the non-multiplexing control
422 system, which can be explained by the lower input impedance of these chips. However, the
423 signal waveforms and the wave shapes of the extracellular spikes were virtually identical.
424 The mean difference between the normalized spike waveforms of a well-isolated test single
425 unit, recorded by the current and the control system, was 10% of the standard deviation of
426 the waveform recorded by the control system. The common noise component across
427 channels in the recorded LFPs was significantly lower, especially in the lower frequency
428 ranges, which is presumably a result of the serial transmission of the channels in the
429 multiplexed line instead of the non-multiplexed parallel transmission. The intra-shank
430 correlation of the recorded signals (i.e., the mean of the correlation values calculated
431 between pairs located on the same shanks; see MATERIALS AND METHODS) was
432 similar in both systems for every investigated frequency range. However, the mean
433 correlation across the shanks gradually decreased at higher frequencies in our system
434 ($R=0.8, 0.72$ and 0.23 for $>1, >10,$ and >100 Hz respectively), while slightly increased for
435 the control system ($R=0.55, 0.72, 0.75$). The single unit yield was larger in our system,
436 despite the slightly lower signal amplitude, and lower sampling rate (20 kS/s vs. 34 kS/s).

437 After the automatic spike extraction and clustering of the sample session recorded by both
438 systems (see MATERIALS AND METHODS), 26 and 7 single units were detected on a
439 single shank, using our (test) and the control systems, respectively. After taking account of
440 cluster quality criteria, nine vs five clusters, respectively, satisfied our ‘conservative’
441 criteria (see MATERIALS AND METHODS).

442

443 **Physiological Recordings**

444 *Electro-anatomy of cortical layers*

445 We have implanted the high-density, 256-site probes in 5 rats. In two rats, two probes were
446 implanted (512 channels). In one rat the probes were placed in the same hemisphere,
447 whereas in the other animal they were placed symmetrically in the two hemispheres (Fig.
448 2).

449

450 The relationship between laminar arrangement of afferents and the characteristic depth
451 profiles of various oscillatory and irregular LFP patterns can offer means for an
452 identification of the various cortical layers and their transitions (Buzsaki et al. 2012;
453 Montgomery et al. 2008). Here we illustrate our strategy in the hippocampus, whose
454 laminar structures and well-understood LFP patterns allow for an online quantitative
455 identification of each of the recording electrode sites (Montgomery et al. 2008).

456

457 First, each of the 256 LFP signals were filtered by a narrow gaussian band-pass filter (peak
458 = 300 Hz, SD = 10 Hz) and power values, determined from a randomly sampled 1-sec
459 epoch, are displayed for each of the 256 sites as a 2-dimensional map (Fig. 5A). This
460 frequency band was empirically determined by selecting a frequency band with the largest
461 ratio of power between cell body layers and dendritic layers (Fig. 6). The band we selected
462 (300 Hz Gaussian filter, SD = 10 Hz) presumably represents various aspects of multi-unit
463 activity (Ray and Maunsell 2011), since its spatial distribution clearly marked the
464 pyramidal layer and the dentate-hilar area, as reflected by the density of the recorded units.
465 The soma location of the recorded neurons was estimated by the largest amplitude
466 waveform representing the firing of each unit (Csicsvari et al. 2003; Fujisawa et al. 2008)

467 and assigned to the recording site of the relevant shank in the electro-anatomical map (Fig.
468 5A). In the next step, coherence maps in the gamma frequency band (40-90 Hz) were
469 constructed. Each site served as a reference and coherence distribution with each of the
470 remaining 255 sites was determined iteratively (Montgomery et al. 2008) (Fig. 5B and 7A).
471 Using a gradient-descent algorithm (Fig. 7), the recording sites were clustered based on the
472 resulting coherence matrix, and the resulting coherent channels were grouped together.
473 Next, a two-dimensional gamma coherence map was generated (based on the spatial
474 locations of the recording sites and their coherence cluster identities) and combined with
475 the power map (Fig. 5C) to identify the cellular layer amongst the emerging clusters. The
476 boundaries of the channel clusters happened to be nicely overlapping with the anatomical
477 layers without any *a priori* knowledge of the histological control. In a different display,
478 each recording site was connected to its most coherent neighbor on the adjacent shanks.
479 The connecting lines were colored-coded on the basis of cluster identity of their leftmost
480 member site. The resulting ‘coast-line’ display provided a smooth layer-specific map of the
481 recorded space by the silicon probe (Fig. 5C, right). The electro-anatomical map
482 constructed from unit firing and LFP signals corresponded faithfully to the histological
483 reconstruction of the electrode tracks and the anatomical layers of the hippocampus (Fig.
484 5D).

485 High-density silicon probe recordings in the neocortex were similarly advantageous for
486 cortical layer identification. Gamma coherence reliably identified three separate layers,
487 corresponding to the superficial (II/III), middle (IV) and deep (V/VI) layers (Fig. 8A).

488

489 *Large-scale recording of unit activity*

490 Figure 8B shows wide-band (0.5 Hz – 10 kHz) traces from a single shank in the
491 somatosensory cortex. Neurons were recorded from all shanks of the probes in both
492 hemispheres for several days before advancing the probes into the hippocampus. In
493 conjunction with LFP, population patterns of unit firing allowed for a clear classification of
494 brain states (Fig. 8C).

495 Neocortical and hippocampal units were clustered semi-automatically (Harris et al. 2000),
496 followed by physiological classification of the units into putative principal cells and

497 interneurons (Bartho et al. 2004; Fujisawa et al. 2008). To obtain an ‘at glance’ information
498 about the recorded neurons, an algorithm was designed to summarize the main
499 physiological and behavioral correlates of each unit (Fig. 9). First, the mean waveform of
500 the unit recorded at multiple sites is displayed, together with wave shape classification of
501 the unit, and its autocorrelogram and interspike interval histogram. The next level of
502 analysis characterizes the spike-LFP relationships. In case of hippocampal neurons, the
503 preferred firing phase in relation to theta, gamma and ripple oscillations of the unit are
504 displayed, together with sharp-wave related firing (Fig. 9). The third level of analysis
505 shows the neurons’ behavioral correlates, such as its place related firing in the maze and
506 spike phase precession relative to the theta rhythm (Fig. 9). The display panels can be
507 flexibly replaced with other analyses, such as displaying the anatomical location of the
508 neuron in two-dimensional space, its cluster space relative to surrounding clusters, brain
509 state-dependence of firing rates and cross-correlation with selected other neurons.

510

511 The 256-site probe was designed for large spatial coverage to allow monitoring the activity
512 in multiple hippocampal layers. This inevitably compromised the density of the recording
513 sites (50 μm) and, consequently, reduced the unit clusters with high isolation quality
514 (MATERIALS AND METHODS) compared to higher density (20 μm spacing) probes.
515 However, the lower unit yield per site was offset by the 256-site probe’s ability to record
516 from multiple layers (Fig. 10)

517

518 Large-scale recording from local circuits has the power of identifying monosynaptic
519 connections, at least between principal cells and interneurons (Fujisawa et al. 2008). This is
520 typically done by examining counts of co-occurrences of spiking in the putative pre- and
521 postsynaptic neurons, as exemplified by the large peaks at short latency time lags (Fig.
522 11A, B). Our analysis is limited only to pyramidal-interneuron interactions, since the
523 validation of the monosynaptic peaks on the cross-correlograms of the pyramidal-pyramidal
524 neurons pairs was not reliable due to their low firing rates. However, with extended
525 recordings and increased number of spikes, the circuit analysis can be extended to
526 pyramidal-pyramidal connections as well (Hirabayashi et al. 2013). Of the 26,406 possible

527 connections of a total of 163 simultaneously recorded neurons (counting each literal pair
528 twice, corresponding to the two directions) recorded by two probes (512 sites) in the same
529 hippocampus (Figure 11A, B), 137 pairs (0.005%; marked red in Fig. 11C) had short
530 latency (<5 ms onset) and narrow significant peaks (<2 ms) or troughs in their cross-
531 correlograms, indicating that the presynaptic partner neuron was an excitatory or inhibitory
532 neuron, respectively. In most cases, the postsynaptic targets were interneurons, as judged
533 by their high firing rates and waveforms (Sirota et al. 2008). Most functionally connected
534 pairs were detected locally in the same hippocampal region but several connections were
535 detected between neurons in the CA3 and CA1 regions as well (Fig. 11). Several pyramidal
536 cells of both local and distant origin could converge on the same putative interneuron.

537

538 Increasingly larger numbers of simultaneously recorded neurons also facilitates the search
539 for spatiotemporal patterns of neuron interactions in local circuits because the likelihood of
540 finding connected pairs increases quadratically with the number of the recorded cells
541 (Bartho et al. 2004; Carandini 2012). Since the spike transmission probability (i.e., the
542 excess numbers of postsynaptic spikes divided by the number of presynaptic spikes,
543 reflecting the efficacy of spike transfer function) can be used as an indirect measure of
544 synaptic strengths between neurons (Fujisawa et al. 2008), the magnitude of spike transfer
545 can be used in future studies to estimate the state and task-related circuit reconfigurations
546 (Fujisawa et al. 2008).

547

548 *State-dependent activation of single neurons by multiple inputs*

549 In the intact brain, neurons are embedded in interconnected networks and respond with
550 spikes to a single input or a combination of inputs. Since afferents to hippocampal neurons
551 target specific layers, high-density recordings from multiple layers and regions can, in
552 principle, track the activity of the afferents giving rise to each spike. To illustrate the
553 principle, we sampled LFP multiple times at all recording sites in 20-msec windows,
554 centered on the spikes of a CA1 pyramidal neuron during sharp wave-ripple events and
555 ambulation while the rat was walking through the place field of the neuron (O'Keefe and

556 Nadel 1978) (Fig. 12; Supplemental movie 1). Sharp wave-ripples are self-organized
557 population patterns that arise in the CA3 region and depolarize the mid-apical dendrites of
558 CA1 neurons, as seen extracellularly by a large amplitude negative wave in stratum
559 radiatum (Ylinen et al. 1995). As expected, LFP activity prior to the occurrence of spikes
560 during sharp wave-ripple events was most prominent in the CA1 stratum radiatum (Fig.
561 12A; Supplemental movie 1). In contrast, during place-related activity pyramidal cells are
562 believed to be discharged by a combination of the direct entorhinal input terminating in
563 stratum lacunosum-moleculare and the CA3 input (Moser et al. 2008) (Fig. 12B). During
564 ambulation, LFP activity prior to spike occurrence was first observed in the stratum
565 lacunosum-moleculare and dentate molecular layer, followed by the CA3 activation in CA1
566 stratum radiatum prior to the spikes of the place cell. These findings illustrate the
567 exceptional power of the combination of recording spikes and high spatial density
568 monitoring of LFP for understanding the input-output transformation of single neurons.

569

570 *Large-scale recordings from the mouse brain*

571 Multiplexing neuronal signals is even more critical for recordings from mice because the
572 size and weight of the preamplifiers and the connecting cable can seriously affect the
573 behavioral performance of the animal. Either 32-channel or 64-channel head stages and
574 their combinations are deployed for high-density recordings from two or three brain
575 structures, including various neocortical areas, hippocampus, thalamus, nucleus accumbens
576 and ventral tegmental area. In addition to the multiplexed outputs, the recording head stage
577 contains two detachable LEDs for tracking the animal's position with a video camera and a
578 3-dimensional accelerometer to monitor fast head movements. Figure 13A shows
579 illustrative neocortical traces from a mouse exploring an open maze. The silicon probe
580 recordings are most often combined with optogenetic manipulation of the recorded neurons,
581 using laser or LED-powered sharpened optical fibers that deliver light to the tips of the
582 probe shanks (Berenyi et al. 2012; Royer et al. 2010; Stark et al. 2012) (Fig. 13B).

583

584 **DISCUSSION**

585 We have described a complete system that allows high channel count recordings from a

586 small volume of neuronal tissue using a lightweight signal multiplexing head-stage that
587 permits free behavior, such as exploration in mazes. This was achieved by multiple stages
588 of development, including multishank high-density recording silicon probes, ultra-flexible
589 interconnect, miniaturized microdrive (Vandecasteele et al. 2012) and, most importantly,
590 high throughput on-stage signal multiplexing, remote-site digitization and demultiplexing,
591 which allow to link the animal to the recording/processing hardware by an ultra-light cable.
592 The system has been extensively tested for large-scale recordings of spike outputs and LFP
593 signals in both rats and mice. The two-dimensional distribution of the recording sites
594 distributed across several layers and regions can provide important information about the
595 distribution of LFP together with large-scale unit recordings

596 Sensing of electrical activity is complementary to optics-based imaging methods
597 (Alivisatos et al. 2013). Silicon probes can access deep brain structures and offer sampling
598 speed at the level of neuronal communication. They provide neuron-scale resolution in
599 local circuits and permit the study of interactions of multiple brain regions, currently not
600 practical with imaging methods (Ghosh et al. 2011). Electrodes are invasive, a feature that
601 can be improved with further size reduction, refinement of tip configuration and tissue
602 compatible coating (Du et al. 2011; Kipke et al. 2008; Wise et al. 2004). In the current
603 configuration, the combined volume of the eight recording shanks of the 256-site probe is
604 comparable to the volume of eight wire tetrodes (Wilson and McNaughton 1993) but it can
605 record from significantly larger numbers of units in addition to providing high-spatial
606 resolution LFP signals. Even the eight-shank 64-site probe can record from >100 neurons
607 (Fujisawa et al. 2008). In addition, linear probes have the advantage of online identification
608 of the recording layers, the spatial localization of the main current sources and sinks and the
609 positions of the recorded neurons (Csicsvari et al. 2003). We present here a method to
610 determine the position of the electrodes during experiments, exploiting the high within-
611 layer gamma band coherence of the LFP. Polarity reversal of sleep spindles, K complexes
612 and other LFP patterns can also be used to increase the precision of layer segregation. Since
613 the layer identification we described is done in situ, it allows for the determination of the
614 recordings sites in each session. This is a major advantage in experiments when the probe is

615 moved gradually in the course of multiple sessions and for layer-restricted optical
616 stimulation in future experiments.

617 The 50- μm spacing of the recording sites on the 256-site probe (Fig. 1A and Fig. 10.) is
618 suboptimal for unit recordings and cell clustering (Harris et al. 2000). Denser recording
619 sites without increasing the shank volume is desirable. On the other hand, the additional
620 two-dimensional recording of the LFP from multiple layers and regions is an additional
621 benefit. Due to the rapid development of silicon technology, probes with >1000 site counts
622 and 20 μm site spacing, yet without further size increase, are expected in the near future.
623 Ultimately, a dynamically reshapeable probe design (by selecting recording sites within the
624 cellular layers with high quality unit activity) would overcome the tradeoff of the current
625 probe design, by significantly improving the single unit yield and still keeping the amount
626 of recorded data reasonable at the same time.

627

628 In addition to significantly increasing the number of recording sites, the size of the
629 multiplexers should also be considerably reduced. Although the size and weight of the
630 extracranial devices is less of a problem in head-fixed animals, currently they are the most
631 limiting factors in experiments that require free movement of small rodents. In the current
632 configuration, silicon probes are connected to the multiplexers via an ultraflexible
633 polyimide cable but the multiplexers have to be manually soldered onto the printed circuit
634 board. In addition to size limitation, the numerous mechanical connections between the
635 probe, interconnect, multiplexers and the offsite demultiplexer increase failure rate.

636 In terms of the cluster quality of units, our system outperformed a benchmark commercial
637 recording system. The relatively low input impedance of the INTAN RHA-2132
638 multiplexer chip (13 $\text{M}\Omega$ at 1 kHz) and its relatively high input capacitance (12 pF)
639 attenuated the recorded signal by approximately 20%, comparing with another non-
640 multiplexed headstage. However the serial, temporally non-coincident transmission of the
641 multiple channel segments make the multiplexer more resistant to mechanical cable
642 artifacts. Signal attenuation of the multiplexer could be eliminated by adding buffer
643 operational amplifiers before multiplexing. However, such modification may double the

644 current size of the multiplexer, adding unwanted additional weight and volume to the
645 headstage.

646

647 New generation probes may have on-probe signal amplification and multiplexing
648 capabilities (Csicsvari et al. 2003; Olsson et al. 2005). Alternatively, the required signal
649 multiplexing circuits can become an integral part of the flexible interconnect cable (Viventi
650 et al. 2011). The use of flexible and active interface electronics may offer an alternative
651 approach that may be advantageous for several applications. The digital output of the
652 multiplexers (Harrison 2008) allows direct streaming of the neurophysiological data to the
653 computer without the extra step of analog-digital conversion. Digital multiplexers also offer
654 noise reduction since potential noise sources of cable transmission, further amplification
655 and offsite digital conversion can be eliminated (Harrison 2008). In principle, amplification
656 and multiplexing can be placed on the probe shanks, effectively reducing the required large
657 numbers of interconnects between the recording sites and electronics outside the brain.
658 Unfortunately, current CMOS circuits require ~ 1 V supply voltage and may generate both
659 excess heat and local electric fields that may modify the activity of nearby neurons if
660 placed on the shank itself (Berenyi et al. 2012). Thus, without dramatic reduction the power
661 consumption, brain embedded electronics remains a major challenge (Alivisatos et al.
662 2013).

663

664 In principle, cables interconnecting the head stage and the recording system can be
665 completely eliminated by telemetry. While up to 64-channel telemetry systems have been
666 successfully used in small animals (Greenwald et al. 2011; Harrison et al. 2011; Sodagar et
667 al. 2007; Szuts et al. 2011) and may be the only solution for specific applications (Yartsev
668 and Ulanovsky 2013), multiplexing and ultraflexible cables allows much higher bandwidth,
669 higher channel counts and lower noise. The power source required for telemetry adds
670 additional weight and limit the duration of the experiments, especially in mice.

671

672 Computation in brain circuits is performed by numerous specialized neurons. Identification
673 and manipulation of specific neuron types in the behaving animal has recently become

674 possible with optogenetics (Boyden et al. 2005), combined with ever-increasing specificity
675 of neuron labeling, mostly in mice (Madisen et al. 2012; Taniguchi et al. 2011). Therefore,
676 perhaps the most important new direction should be the development of combined
677 techniques that allow precise delivery of light locally to the simultaneously recorded
678 neurons. Experiments have shown that as low as 5-15 μ W of light is sufficient to activate
679 ChR2-expressing neurons in vivo (Stark et al. 2012). However, construction and use of
680 silicon probe devices with etched optical fibers that allow precise local delivery of light
681 energy is currently done manually and only few laboratories have the capability to use such
682 methods routinely (Anikeeva et al. 2012; Royer et al. 2010; Royer et al. 2012; Stark et al.
683 2012). To bridge the gap between optogenetics and large-scale recording of neurons, there
684 are at least two possible viable solutions. The first one is adding optical waveguides
685 integrated into the shanks of the silicon probe and coupling the back end of the waveguides
686 to lasers, LEDs or laser diodes (Stark et al. 2012; Wu et al. 2013; Zorzos et al. 2010). The
687 second option is integrating neuron-size LED sources mixed with the recording sites on the
688 silicon probe (Kim et al. 2013). Either configuration will offer unmatched spatial precision
689 and capability of targeted perturbation and recording from specified neuron types.
690 Integration of optical stimulation, large-scale recording and on-stage multiplexing will
691 facilitate the dissemination and use such tools in a large number of laboratories for the
692 investigation of multiple circuits and their behavior-dependent interactions in freely
693 moving small rodents for testing hypotheses of neural networks and brain function.
694

695 **Figure legends**

696 **Figure 1.** System overview. **(A)** High channel count (256 sites) silicon probe connected to
697 a printed circuit board via a flexible polyimide ribbon cable. The printed circuit board
698 contains 8 separate 32-channel signal multiplexers (4 on each side) and accessory circuit
699 elements. **(B).** A simulated headstage input signal illustrating a spike waveform on one of
700 the 32 channels, and various levels of DC on the remaining 31 channels (1 ms). **(C)** Time-
701 shared multiplexed signal transmitting the 32 channels shown in b. **(D)** Circuit schematics
702 and working principle of the multiplexer and a zoomed segment of the time epoch shown
703 by rectangle in c. The multiplexer chip receives the input signals and is driven by both the
704 main microcontroller's clock signal and the complementary clock bits generated by the
705 clock divider. The horizontal line separates circuits contained in the head stage and the
706 main box. Middle part: zoomed segment of the multiplexed signal shown in b. The reset
707 line resets the clock bits to '00000' after every 32 steps to ensure the proper channel order.
708 The trigger signal is timed to sample the 'tail' of each transmitted signal snippet (marked
709 by black triangles). The two large steps (red) correspond to the two digital samples at the
710 trough of the spike waveform on input channel 3. Right part: Numeric representation of the
711 analog-to-digital converted multiplexed line (readout from the A/D card), and its
712 demultiplexed form after the software reconstruction of the digitized samples.

713

714 **Figure 2.** Surgery details of probe implantation. **(A)** and **(B)**, skull coordinates for
715 implantation of two 256-site probes into the same **(A)** or two hemispheres **(B)**. The
716 orientation of the probe shanks is indicated by pink lines, next to the probe drives. Black
717 dots, watch screws. GND, ground. REF, reference electrode. **(C)** During probe implantation
718 the probe and the PC board are rigidly connected by brass rods and the assembly is held by
719 an alligator clip. The probe is fixed to the drive and connected to the PC board by a flexible
720 polyimide cable. **(D)** The head stage after implantation. The output connector,
721 accelerometer and the copper wire mesh shield are marked by arrows. **(E).** Details of the
722 probe shanks after they penetrated the brain. A, anterior; P, posterior direction. Bottom, top
723 view of the implanted drives. **(F).** Rat equipped with two 256-site probes during maze
724 exploration connected to the equipment via an ultra-flexible cable (yellow).

725 **Figure 3.** Head stage multiplexers. **(A)** and **(B)** 32 and 64-channel multiplexers with high
726 density Omnetics connectors. **(C)** 64-site probe bonded to a 64-channel multiplexer. **(D)**
727 Circuit schematics representing the electrical components and wiring scheme of the 32
728 channel multiplexer. Top: wiring diagram of the INTAN RHA-2132 multiplexer chips and
729 the high-density Omnetics connector for electrode interfacing. The cutoff frequencies of the
730 low and highpass filters are set with the three resistors on the left. Bottom: Supplementary
731 electronics to provide clock bits and buffer the signal. Top row (left-to-right): 9-pin
732 Omnetics connector interfaces with the main box; high-speed dual buffer operational
733 amplifier. Bottom row: synchronous clock divider chip; external LED power port for
734 position tracking; clock inverter chip with Schmitt trigger; decoupling capacitor.

735

736 **Figure 4.** Demultiplexer circuit. **(A)** Working principle of the real time demultiplexer. The
737 clock signal from the main box (Fig. 1) is successively halved 4 times to produce 4
738 subsequent clock bits (blue trace, Bc1..5). A clockbit-mask pattern set by the user interface
739 (Bm1..5, red traces) is pairwise-compared (XNORed) with the clock bits, and the results
740 are logically ANDed. The output of this logical operation is the trigger (pink trace) which
741 switches the sample-and-hold circuit so that when the clock bits match the preset mask the
742 circuit works as a relay ($1/32^{\text{th}}$ of the running cycle); otherwise it holds the last sampled
743 voltage ($31/32^{\text{th}}$ of the running cycle). The output of the sample-and-hold circuit is shown
744 as red and blue lines for the sampling and holding periods, respectively. The example
745 demultiplexes channel 2. The demultiplexed signal trace is low-pass filtered to remove the
746 step functions, and optionally high-pass filtered at 500 Hz to separate unit firing from the
747 LFP. **(B)** Temporal delay of the demultiplexing process. Red trace: original input
748 waveform; blue trace: output of the sample and hold circuit; green trace: low-pass filtered
749 signal at the output of the demultiplexer. **(C)** Signal transmission characteristics of the
750 demultiplexer for a large-amplitude step function. Red trace: original input signal; upper
751 green trace: demultiplexed waveform; lower green trace: demultiplexed signal on an
752 adjacent channel in the multiplexed sequence. Note the different amplitude scales for the
753 traces. **(D)** Single trace examples of a demultiplexed unit. The upper two traces represents
754 two waveforms representing two distinct projections of the spike onto two adjacent

755 recording sites of the probe. The bottom trace shows the signal recorded on neighboring
756 channel in the multiplexed stream. (E) Spike-triggered average waveforms of the neuron
757 shown on panel (D). Note the lack of crosstalk in both the temporal (incomplete signal level
758 settling during multiplexing or demultiplexing, third trace) and spatial (crosstalk across
759 leads, fourth trace) domain.

760

761 **Figure 5.** Electroanatomy of the hippocampus. (A) Distribution of high frequency power
762 (300 ± 10 Hz) on each of the 256 sites of the silicon probe. The 32 x 8 color matrix is a
763 representation of the 256-site probe shown in Fig. 1A. Each rectangle represents a $300\ \mu\text{m}$
764 (intershank distance) by $50\ \mu\text{m}$ (vertical intersite distance) area to mimic the 2-dimensional
765 geometry of the probe coverage. Clustered neurons, assigned to the largest amplitude
766 recording sites, are superimposed on the power map. (B) Coherence maps of gamma
767 activity (30-90 Hz). The ten example sites (black dots) served as reference sites and
768 coherence was calculated between the reference site and the remaining 255 locations for a
769 one second long recording segment (Fig. 7). Middle, composite figure of the combined
770 coherence maps (see also Fig. 7). (C). Two-dimensional combined map of gamma
771 coherence and high frequency power distribution. Right, coastline map of layer-specific
772 coherence contours. (D) Histological reconstruction of the recording tracks (arrows). The
773 shifting of the tracks in the neocortex is due to a slight displacement of the
774 neocortex/corpus callosum relative to the hippocampus during the tissue sectioning process.
775 Right, physiology-based map superimposed on the recording tracks.

776

777 **Figure 6.** Layer-specific LFP power distribution of various frequency bands in the
778 hippocampus. The arrangement of each panel is the same as Fig. 3A. Each panel is showing
779 the power map of the same representative, one second-long recording segment containing
780 sharp-wave ripples. For details on filtering, see MATERIALS AND METHODS.

781

782 **Figure 7.** Coherence based clustering of electrode sites. (A) Cross-coherence-matrix of
783 the recorded 256 channels calculated from a randomly selected 1-sec long recording
784 segment. (B) and (C) Evolution of coherence clusters during clustering procedure. Initially

785 (T=1), electrode sites, represented by rectangles, distributed randomly among 10 clusters
786 denoted by different colors of the rectangles. T denotes the number of algorithmic steps.
787 During each step the algorithm examines whether reassignment of one randomly chosen
788 electrode site into another randomly chosen cluster would increase the clusters mean
789 coherence or not. If it increases the cluster's mean coherence, the site is merged into the
790 cluster. During the iterative reassignments clusters emerge and stabilize. Stability is shown
791 by the negligible changes between 10000 and 40000 iterations. Panel B represents the
792 clustering for a sleep session (sharp wave event), while panel c is created from a random
793 sample during exploratory behavior (theta).

794

795 **Figure 8.** Electroanatomy of the neocortex (A) Combined coherence map of gamma
796 activity (30-90 Hz), as in Fig. 5B. Each site served as a reference and coherence was
797 calculated between the reference site and the remaining 255 locations. The resulting
798 combined map is superimposed on the histologically reconstructed tracks in the
799 sensorimotor cortex. Note reliable separation of layer IV, superficial and deep layers and
800 the lack of a 'layer IV' coherence band in the adjacent motor cortex (shanks 6 to 8). (B)
801 300 ms long raw signal traces of a shank spanning across multiple layers of the cortex,
802 showing spike activity of multiple neurons. (C) Relationship between the activity patterns
803 of multiple neurons and the local field potential during a sleep spindle episode. The
804 recording site of the LFP trace in marked by * on the top of the panel in A. Figure is a
805 representative sample for illustration purposes only.

806

807 **Figure 9.** Characterization of single units. (A) Orientation of two probes placed in the same
808 hippocampus in the transversal (T) and longitudinal (L) axes (see also Fig. 2A). Histological
809 reconstruction of the recording probe shanks with superimposed traces of a sharp wave
810 ripple event (300 msec). The tissue slices were cut parallel with the probe shanks, i.e.,
811 perpendicular and parallel with the longitudinal axis of the hippocampus. (B)
812 Characterization of 4 different units recorded from the sites marked by the red arrows. First
813 row of each panel shows: (1) Two-msec traces of a hippocampal single unit recorded from
814 multiple sites of the shank. (2) Classification of unit clusters, recorded in a single session,

815 on the basis of their trough-to-peak duration versus spike width at 20% of the trough
816 magnitude. The relevant unit is indicated by a red dot. (3) Autocorrelogram and burstiness
817 index, determined as the ratio of spikes at <8 msec intervals divided by all spikes (Mizuseki
818 et al. 2009) and (4) interspike interval (ISI) histogram (log scale). Second row: Cross-
819 correlation between LFP and unit firing, showing separately for theta (4-12 Hz), gamma
820 (30-90 Hz) and sharp wave-ripple (SWR; 120-250 Hz). Preferred phase of firing is also
821 shown numerically. Phase zero corresponds to trough. Last panel, SWR-related firing of
822 the unit. The duration of the SWR is normalized. The modulation index (MI), defined by
823 difference/sum of the firing rate during and outside ripples, is shown above the panel. Third
824 row: Position-dependent firing rates ('place cell' activity) during left and right journeys in
825 the maze and corresponding spike-phase relationship to position within the largest place
826 field (red lines).

827

828 **Figure 10.** Comparison of single-unit isolation metrics. Each measure is shown for six
829 different recording conditions (probe, structure, species) **(A)** and **(C)** Mahalanobis distance
830 of isolated spike clusters in high dimensional feature space. **(B)** and **(D)** Contamination of
831 isolated single-unit clusters, calculated as the ratio of spikes occurring within (2 ms) and
832 after (20 ms) the refractory period of the given neuron. Medians and the interquartile ranges
833 are shown. N denotes the number of neurons fulfilling the inclusion criteria.

834 Panels **A**, **B** and **C**, **D** display the same dataset using permissive and conservative inclusion
835 criteria, respectively. Abbreviations: Hip: hippocampus; Cx: cortex; 2x256: two 256
836 channel silicon probe with multiplexing headstage; 64: Buz64-type silicon probe with 20
837 μm inter-site distance with multiplexing headstage; 64Sp: Buz64Sp-type 6 shanks silicon
838 probe, with 20 μm inter-site distance equipped with an optical fiber on each shank,
839 recorded by a non-multiplexing headstage and amplifier.

840

841 **Figure 11.** Partial circuit reconstruction from physiological interactions. **(A)** Identification
842 of monosynaptic connections. Only pyramidal-interneuron connections are shown.
843 Autocorrelogram of the reference (presynaptic) neuron (pre), referred (postsynaptic) neuron
844 (post) and cross-correlogram (CCG) between the neuron pair. Short-latency (<1 ms) narrow

845 peak (arrow) identifies the reference cell as a putative excitatory (pyramidal) neuron. Blue
846 line, mean of time-jittered spikes; red line, point wise comparison ($P < 0.01$); magenta line,
847 global comparison ($P < 0.01$; for explanation, see Methods; ref Fujisawa et al., 2008). (B)
848 Same as in (A) from another pair with members recorded from the CA3 and CA1 regions.
849 (C) Cross-correlogram matrix based on 26406 simultaneously recorded neuron pairs ($n =$
850 163 neurons) in a single session. Red pixel, monosynaptic connection (based on significant
851 short-latency peaks) with reference neuron as putative pyramidal cell ($n = 127$). White
852 lines, separation of neurons recorded by probe 1 and probe 2. Numbers identify the
853 recording shanks. Cross-correlograms shown in A and B are circled. (D) Circuit diagram
854 reconstructed from monosynaptic connections (for shank orientation, see Fig. 2). Red
855 triangles, excitatory neurons. Blue circles, putative inhibitory interneurons. Gray squares,
856 unidentified neurons. Local and CA3-CA1 connections (as shown in A and B) are
857 highlighted by yellow. Note convergence of multiple pyramidal cells on target
858 interneurons. Figure is a representative sample for illustration purposes only.

859

860 **Figure 12.** Spikes are embedded in unique and spatially distributed LFP. Spike-triggered
861 averages of the LFP in the hippocampus during slow-wave sleep (top panel) and
862 exploration (bottom panel). During sleep, spikes were sampled during sharp wave-ripples
863 (SWR); during exploration (theta), spikes of the same neuron were sampled while the rat
864 ran on a linear track for a water reward. Recordings were made by two eight-shank (300
865 μm intershank distance), 256-site silicon probes. The LFP was smoothed and interpolated
866 both within and across shanks. The LFP was triggered by the spikes of a pyramidal neuron
867 in CA1 pyramidal layer (pyr; shown by a star). Both frame sequences show four, 50 μs
868 snapshot of the LFP map before (-3 ms to -1 ms) and at the time of the spike occurrence (0
869 ms). The two images of each frame are showing the activities on the two probes (as shown
870 in Fig. 9). Note that during sleep (top panel), activity arises (negative wave, hot colours) in
871 CA3 and invades the CA1 stratum radiatum (rad). During exploration (bottom panel), the
872 spike is associated with synaptic activity mainly in the stratum lacunosum-moleculare (lm;
873 shown by an arrow) following by the radiatum layer (rad; double arrow), indicating a
874 combination of entorhinal cortex and CA3 input activation.. The LFP map changes

875 characteristically with time (see Supplemental Movie 1). ori, oriens layer; gc, granule cell
876 layer; hil, hilus.

877

878 **Figure 13.** Unit and LFP recordings from the mouse. **(A)** Chronic recordings from a mouse
879 using an 8-shank 64-site silicon probe. 100 msec epochs from each shank are shown. Inset:
880 headstage with silicon probe, microdrive and 64-channel signal multiplexer, surrounded by
881 copper mesh shielding. The freely moving mouse is connected to the equipment by an
882 ultra-flexible cable. **(B)** Two 4-shank, 32-site probes were placed in the nucleus accumbens
883 (top shanks 1-4) and ventral tegmental area (VTA; bottom shanks 1-4) in a TH-Cre;Ai32
884 mouse, expressing ChR2 in tyrosine hydroxylase-expressing neurons. One of the shanks in
885 the VTA also contained an optical fiber for light delivery (Stark et al. 2012). Note VTA
886 neuronal responses to 472 nm (bottom red trace) laser light stimulation.

887 **Acknowledgments:** Supported by National Institute of Health Grants NS34994, MH54671
888 and NS074015, the Human Frontier Science Program and the J.D. McDonnell Foundation.
889 AB was supported by a Marie Curie FP7-PEOPLE-2009-IOF grant (No. 254780), EU-FP7-
890 ERC-2013-Starting grant (No. 337075), the ‘Momentum’ program of the Hungarian
891 Academy of Sciences and by the Rosztóczy Foundation.

892

893 **Competing financial interests**

894 Antal Berenyi is the founder of Amplipex Ltd., Szeged, Hungary, which manufactures
895 signal-multiplexed head stages and demultiplexing systems. The other authors declare the
896 absence of any commercial or financial relationships that could be construed as a potential
897 conflict of interest.

898

899 **Author contribution:** AB, AL, TDH and GB designed and developed the silicon probe and
900 the electronics; AB and GB designed experiments; AB, AJN, JL, SF, ES and LR conducted
901 experiments; ZS, AB and GB designed and performed analyses; AB and GB wrote the
902 paper with input from other authors.

903

904

905 **References:**

- 906 **Alivisatos AP, Chun M, Church GM, Deisseroth K, Donoghue JP, Greenspan RJ,**
907 **McEuen PL, Roukes ML, Sejnowski TJ, Weiss PS, and Yuste R.** Neuroscience. The
908 brain activity map. *Science* 339: 1284-1285, 2013.
- 909 **Alivisatos AP, Chun M, Church GM, Greenspan RJ, Roukes ML, and Yuste R.** The
910 brain activity map project and the challenge of functional connectomics. *Neuron* 74: 970-
911 974, 2012.
- 912 **Anikeeva P, Andalman AS, Witten I, Warden M, Goshen I, Grosenick L, Gunaydin**
913 **LA, Frank LM, and Deisseroth K.** Optetrode: a multichannel readout for optogenetic
914 control in freely moving mice. *Nature neuroscience* 15: 163-170, 2012.
- 915 **Bartho P, Hirase H, Monconduit L, Zugaro M, Harris KD, and Buzsaki G.**
916 Characterization of neocortical principal cells and interneurons by network interactions and
917 extracellular features. *Journal of neurophysiology* 92: 600-608, 2004.
- 918 **Berenyi A, Belluscio M, Mao D, and Buzsaki G.** Closed-loop control of epilepsy by
919 transcranial electrical stimulation. *Science* 337: 735-737, 2012.
- 920 **Blanche TJ, Spacek MA, Hetke JF, and Swindale NV.** Polytrodes: high-density silicon
921 electrode arrays for large-scale multiunit recording. *Journal of neurophysiology* 93: 2987-
922 3000, 2005.
- 923 **Boyden ES, Zhang F, Bamberg E, Nagel G, and Deisseroth K.** Millisecond-timescale,
924 genetically targeted optical control of neural activity. *Nature neuroscience* 8: 1263-1268,
925 2005.
- 926 **Buzsaki G.** Large-scale recording of neuronal ensembles. *Nature neuroscience* 7: 446-451,
927 2004.
- 928 **Buzsaki G, Anastassiou CA, and Koch C.** The origin of extracellular fields and currents--
929 EEG, ECoG, LFP and spikes. *Nature reviews Neuroscience* 13: 407-420, 2012.
- 930 **Carandini M.** From circuits to behavior: a bridge too far? *Nature neuroscience* 15: 507-
931 509, 2012.
- 932 **Csicsvari J, Henze DA, Jamieson B, Harris KD, Sirota A, Bartho P, Wise KD, and**
933 **Buzsaki G.** Massively parallel recording of unit and local field potentials with silicon-
934 based electrodes. *Journal of neurophysiology* 90: 1314-1323, 2003.
- 935 **Du J, Blanche TJ, Harrison RR, Lester HA, and Masmanidis SC.** Multiplexed, high
936 density electrophysiology with nanofabricated neural probes. *PloS one* 6: e26204, 2011.
- 937 **Du J, Riedel-Kruse IH, Nawroth JC, Roukes ML, Laurent G, and Masmanidis SC.**
938 High-resolution three-dimensional extracellular recording of neuronal activity with
939 microfabricated electrode arrays. *Journal of neurophysiology* 101: 1671-1678, 2009.
- 940 **Fujisawa S, Amarasingham A, Harrison MT, and Buzsaki G.** Behavior-dependent
941 short-term assembly dynamics in the medial prefrontal cortex. *Nature neuroscience* 11:
942 823-833, 2008.

943 **Ghosh KK, Burns LD, Cocker ED, Nimmerjahn A, Ziv Y, Gamal AE, and Schnitzer**
944 **MJ.** Miniaturized integration of a fluorescence microscope. *Nature methods* 8: 871-878,
945 2011.

946 **Greenwald E, Mollazadeh M, Hu C, Wei T, Culurciello E, and Thakor V.** A VLSI
947 Neural Monitoring System With Ultra-Wideband Telemetry for Awake Behaving Subjects.
948 *IEEE transactions on biomedical circuits and systems* 5: 112-119, 2011.

949 **Harris KD, Henze DA, Csicsvari J, Hirase H, and Buzsaki G.** Accuracy of tetrode spike
950 separation as determined by simultaneous intracellular and extracellular measurements.
951 *Journal of neurophysiology* 84: 401-414, 2000.

952 **Harrison RR.** The design of integrated circuits to observe brain activity. *Proceedings of*
953 *the IEEE* 96: 1203-1216, 2008.

954 **Harrison RR, Fotowat H, Chan R, Kier RJ, Olberg R, Leonardo A, and Gabbiani F.**
955 Wireless Neural/EMG Telemetry Systems for Small Freely Moving Animals. *IEEE*
956 *transactions on biomedical circuits and systems* 5: 103-111, 2011.

957 **Henze DA, Borhegyi Z, Csicsvari J, Mamiya A, Harris KD, and Buzsaki G.**
958 Intracellular features predicted by extracellular recordings in the hippocampus in vivo.
959 *Journal of neurophysiology* 84: 390-400, 2000.

960 **Hirabayashi T, Takeuchi D, Tamura K, and Miyashita Y.** Microcircuits for hierarchical
961 elaboration of object coding across primate temporal areas. *Science* 341: 191-195, 2013.

962 **Kim TI, McCall JG, Jung YH, Huang X, Siuda ER, Li Y, Song J, Song YM, Pao HA,**
963 **Kim RH, Lu C, Lee SD, Song IS, Shin G, Al-Hasani R, Kim S, Tan MP, Huang Y,**
964 **Omenetto FG, Rogers JA, and Bruchas MR.** Injectable, cellular-scale optoelectronics
965 with applications for wireless optogenetics. *Science* 340: 211-216, 2013.

966 **Kipke DR, Shain W, Buzsaki G, Fetz E, Henderson JM, Hetke JF, and Schalk G.**
967 Advanced neurotechnologies for chronic neural interfaces: new horizons and clinical
968 opportunities. *The Journal of neuroscience : the official journal of the Society for*
969 *Neuroscience* 28: 11830-11838, 2008.

970 **Lein ES, Hawrylycz MJ, Ao N, Ayres M, Bensinger A, Bernard A, Boe AF, Boguski**
971 **MS, Brockway KS, Byrnes EJ, Chen L, Chen TM, Chin MC, Chong J, Crook BE,**
972 **Czaplinska A, Dang CN, Datta S, Dee NR, Desaki AL, Desta T, Diep E, Dolbeare TA,**
973 **Donelan MJ, Dong HW, Dougherty JG, Duncan BJ, Ebbert AJ, Eichele G, Estin LK,**
974 **Faber C, Facer BA, Fields R, Fischer SR, Fliss TP, Frensley C, Gates SN, Glattfelder**
975 **KJ, Halverson KR, Hart MR, Hohmann JG, Howell MP, Jeung DP, Johnson RA,**
976 **Karr PT, Kawal R, Kidney JM, Knapik RH, Kuan CL, Lake JH, Laramee AR,**
977 **Larsen KD, Lau C, Lemon TA, Liang AJ, Liu Y, Luong LT, Michaels J, Morgan JJ,**
978 **Morgan RJ, Mortrud MT, Mosqueda NF, Ng LL, Ng R, Orta GJ, Overly CC, Pak**
979 **TH, Parry SE, Pathak SD, Pearson OC, Puchalski RB, Riley ZL, Rockett HR,**
980 **Rowland SA, Royall JJ, Ruiz MJ, Sarno NR, Schaffnit K, Shapovalova NV, Sivisay T,**
981 **Slaughterbeck CR, Smith SC, Smith KA, Smith BI, Sodt AJ, Stewart NN, Stumpf KR,**
982 **Sunkin SM, Sutram M, Tam A, Teemer CD, Thaller C, Thompson CL, Varnam LR,**
983 **Visel A, Whitlock RM, Wohnoutka PE, Wolkey CK, Wong VY, Wood M, Yaylaoglu**

984 **MB, Young RC, Youngstrom BL, Yuan XF, Zhang B, Zwingman TA, and Jones AR.**
985 Genome-wide atlas of gene expression in the adult mouse brain. *Nature* 445: 168-176,
986 2007.

987 **Lichtman JW, and Denk W.** The big and the small: challenges of imaging the brain's
988 circuits. *Science* 334: 618-623, 2011.

989 **Logothetis NK.** The underpinnings of the BOLD functional magnetic resonance imaging
990 signal. *The Journal of neuroscience : the official journal of the Society for Neuroscience*
991 23: 3963-3971, 2003.

992 **Madisen L, Mao T, Koch H, Zhuo JM, Berenyi A, Fujisawa S, Hsu YW, Garcia AJ,**
993 **3rd, Gu X, Zanella S, Kidney J, Gu H, Mao Y, Hooks BM, Boyden ES, Buzsaki G,**
994 **Ramirez JM, Jones AR, Svoboda K, Han X, Turner EE, and Zeng H.** A toolbox of
995 Cre-dependent optogenetic transgenic mice for light-induced activation and silencing.
996 *Nature neuroscience* 15: 793-802, 2012.

997 **Mizuseki K, Sirota A, Pastalkova E, and Buzsaki G.** Theta oscillations provide temporal
998 windows for local circuit computation in the entorhinal-hippocampal loop. *Neuron* 64: 267-
999 280, 2009.

1000 **Montgomery SM, Sirota A, and Buzsaki G.** Theta and gamma coordination of
1001 hippocampal networks during waking and rapid eye movement sleep. *The Journal of*
1002 *neuroscience : the official journal of the Society for Neuroscience* 28: 6731-6741, 2008.

1003 **Moser EI, Kropff E, and Moser MB.** Place cells, grid cells, and the brain's spatial
1004 representation system. *Annual review of neuroscience* 31: 69-89, 2008.

1005 **Nicolelis MA, Ghazanfar AA, Faggin BM, Votaw S, and Oliveira LM.** Reconstructing
1006 the engram: simultaneous, multisite, many single neuron recordings. *Neuron* 18: 529-537,
1007 1997.

1008 **O'Keefe J, and Nadel L.** *The hippocampus as a cognitive map.* USA: Clarendon Press,
1009 1978, p. xiv, 570 p.

1010 **Olsson RH, 3rd, Buhl DL, Sirota AM, Buzsaki G, and Wise KD.** Band-tunable and
1011 multiplexed integrated circuits for simultaneous recording and stimulation with
1012 microelectrode arrays. *IEEE transactions on bio-medical engineering* 52: 1303-1311, 2005.

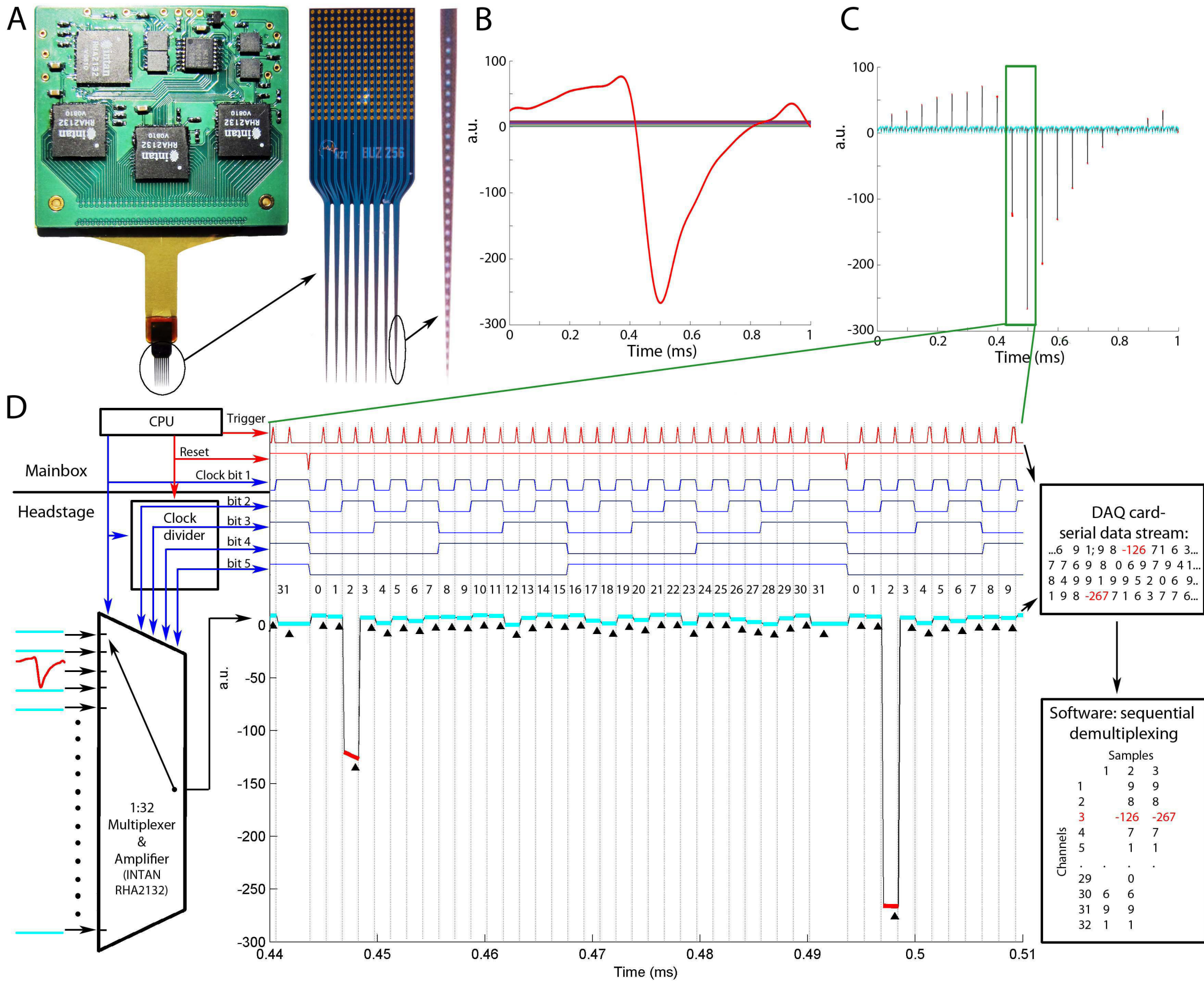
1013 **Prakash R, Yizhar O, Grewe B, Ramakrishnan C, Wang N, Goshen I, Packer AM,**
1014 **Peterka DS, Yuste R, Schnitzer MJ, and Deisseroth K.** Two-photon optogenetic toolbox
1015 for fast inhibition, excitation and bistable modulation. *Nature methods* 9: 1171-1179, 2012.

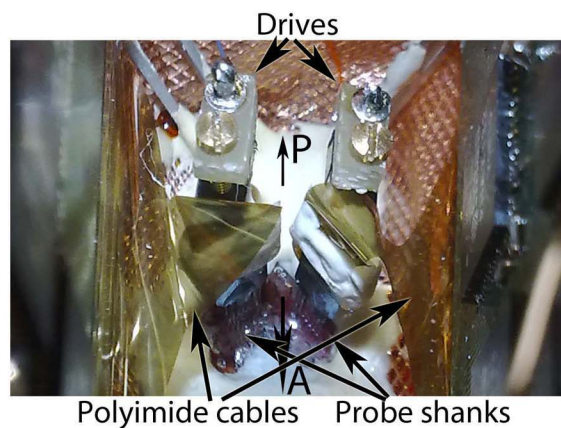
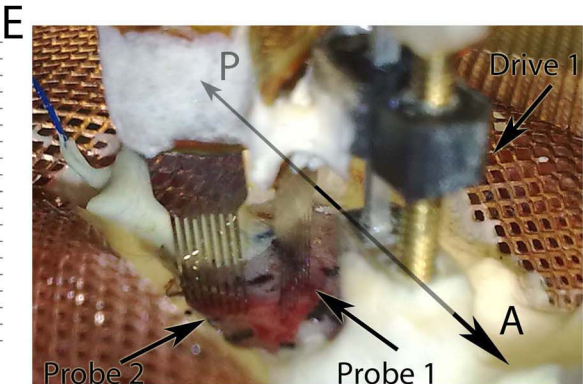
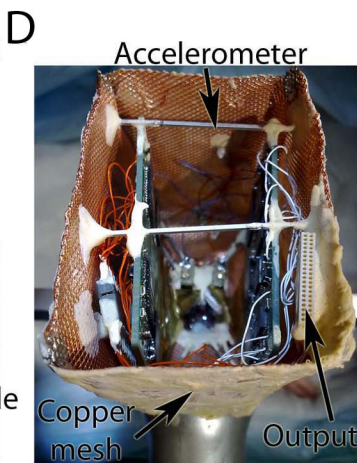
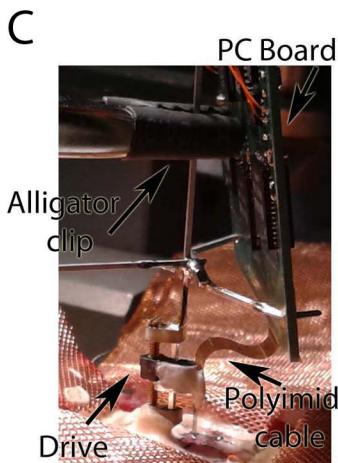
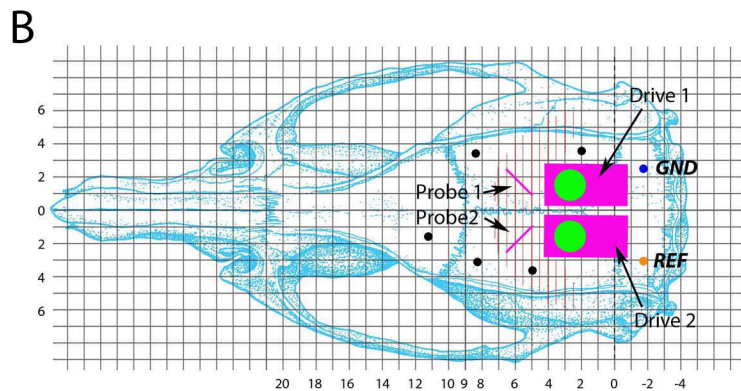
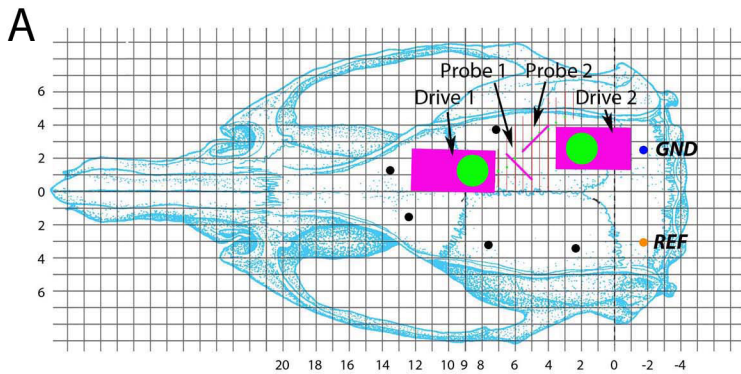
1016 **Ray S, and Maunsell JH.** Different origins of gamma rhythm and high-gamma activity in
1017 macaque visual cortex. *PLoS biology* 9: e1000610, 2011.

1018 **Royer S, Zemelman BV, Barbic M, Losonczy A, Buzsaki G, and Magee JC.** Multi-
1019 array silicon probes with integrated optical fibers: light-assisted perturbation and recording
1020 of local neural circuits in the behaving animal. *The European journal of neuroscience* 31:
1021 2279-2291, 2010.

- 1022 **Royer S, Zemelman BV, Losonczy A, Kim J, Chance F, Magee JC, and Buzsaki G.**
1023 Control of timing, rate and bursts of hippocampal place cells by dendritic and somatic
1024 inhibition. *Nature neuroscience* 2012.
- 1025 **Sirota A, Montgomery S, Fujisawa S, Isomura Y, Zugaro M, and Buzsaki G.**
1026 Entrainment of neocortical neurons and gamma oscillations by the hippocampal theta
1027 rhythm. *Neuron* 60: 683-697, 2008.
- 1028 **Sodagar AM, Wise KD, and Najafi K.** A fully integrated mixed-signal neural processor
1029 for implantable multichannel cortical recording. *IEEE transactions on bio-medical*
1030 *engineering* 54: 1075-1088, 2007.
- 1031 **Stark E, Koos T, and Buzsaki G.** Diode probes for spatiotemporal optical control of
1032 multiple neurons in freely moving animals. *Journal of neurophysiology* 108: 349-363,
1033 2012.
- 1034 **Szuts TA, Fadeyev V, Kachiguine S, Sher A, Grivich MV, Agrochao M, Hottowy P,**
1035 **Dabrowski W, Lubenov EV, Siapas AG, Uchida N, Litke AM, and Meister M.** A
1036 wireless multi-channel neural amplifier for freely moving animals. *Nature neuroscience* 14:
1037 263-269, 2011.
- 1038 **Taniguchi H, He M, Wu P, Kim S, Paik R, Sugino K, Kvitsiani D, Fu Y, Lu J, Lin Y,**
1039 **Miyoshi G, Shima Y, Fishell G, Nelson SB, and Huang ZJ.** A resource of Cre driver
1040 lines for genetic targeting of GABAergic neurons in cerebral cortex. *Neuron* 71: 995-1013,
1041 2011.
- 1042 **Tye KM, and Deisseroth K.** Optogenetic investigation of neural circuits underlying brain
1043 disease in animal models. *Nature reviews Neuroscience* 13: 251-266, 2012.
- 1044 **Vandecasteele M, M S, Royer S, Belluscio M, Berenyi A, Diba K, Fujisawa S,**
1045 **Grosmark A, Mao D, Mizuseki K, Patel J, Stark E, Sullivan D, Watson B, and**
1046 **Buzsaki G.** Large-scale recording of neurons by movable silicon probes in behaving
1047 rodents. *Journal of visualized experiments : JoVE* e3568, 2012.
- 1048 **Viventi J, Kim DH, Vigeland L, Frechette ES, Blanco JA, Kim YS, Avrin AE,**
1049 **Tiruvadi VR, Hwang SW, Vanleer AC, Wulsin DF, Davis K, Gelber CE, Palmer L,**
1050 **Van der Spiegel J, Wu J, Xiao J, Huang Y, Contreras D, Rogers JA, and Litt B.**
1051 Flexible, foldable, actively multiplexed, high-density electrode array for mapping brain
1052 activity in vivo. *Nature neuroscience* 14: 1599-1605, 2011.
- 1053 **Wilson MA, and McNaughton BL.** Dynamics of the hippocampal ensemble code for
1054 space. *Science* 261: 1055-1058, 1993.
- 1055 **Wise KD, Anderson DJ, Hetke JF, Kipke DR, and Najafi K.** Wireless implantable
1056 microsystems: high-density electronic interfaces to the nervous system. *Proceedings of the*
1057 *IEEE* 92: 76-97, 2004.
- 1058 **Wu F, Stark E, Im M, Cho IJ, Yoon ES, Buzsaki G, Wise KD, and Yoon E.** An
1059 implantable neural probe with monolithically integrated dielectric waveguide and recording
1060 electrodes for optogenetics applications. *Journal of neural engineering* 10: 056012, 2013.

- 1061 **Yartsev MM, and Ulanovsky N.** Representation of three-dimensional space in the
1062 hippocampus of flying bats. *Science* 340: 367-372, 2013.
- 1063 **Yizhar O, Fenno LE, Davidson TJ, Mogri M, and Deisseroth K.** Optogenetics in neural
1064 systems. *Neuron* 71: 9-34, 2011.
- 1065 **Ylinen A, Bragin A, Nadasdy Z, Jando G, Szabo I, Sik A, and Buzsaki G.** Sharp wave-
1066 associated high-frequency oscillation (200 Hz) in the intact hippocampus: network and
1067 intracellular mechanisms. *The Journal of neuroscience : the official journal of the Society*
1068 *for Neuroscience* 15: 30-46, 1995.
- 1069 **Zorzos AN, Boyden ES, and Fonstad CG.** Multiwaveguide implantable probe for light
1070 delivery to sets of distributed brain targets. *Optics letters* 35: 4133-4135, 2010.
- 1071
- 1072

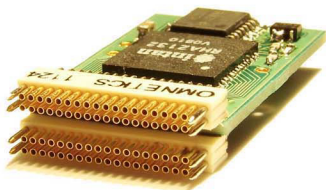




A 32-channel multiplexer



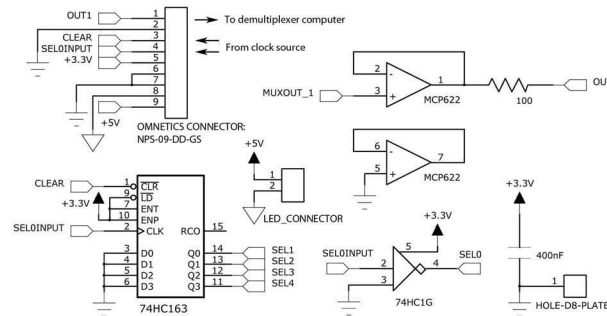
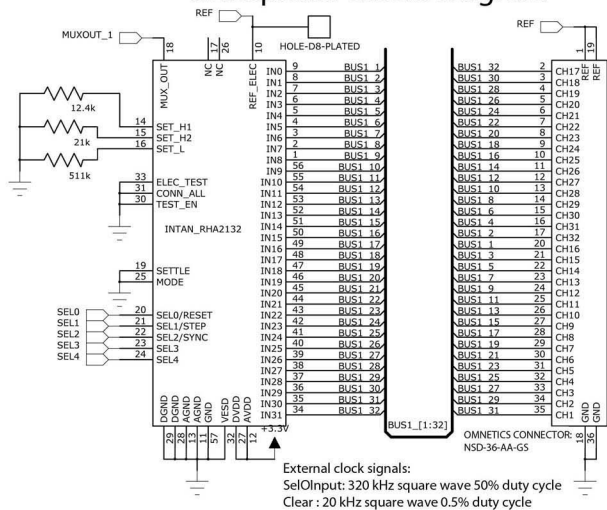
B 64-channel multiplexer

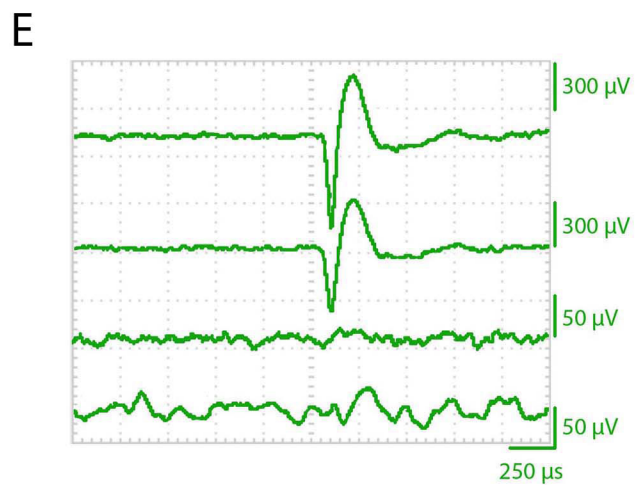
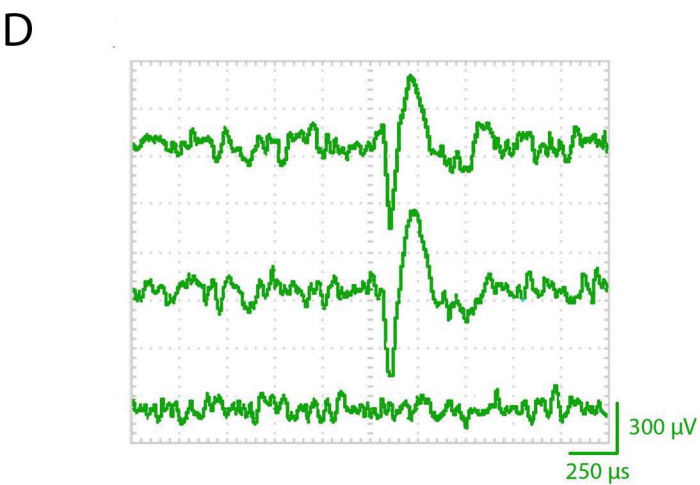
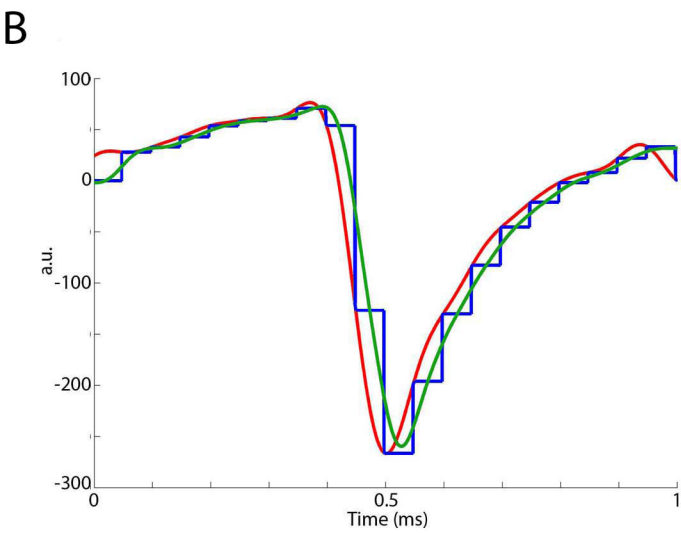
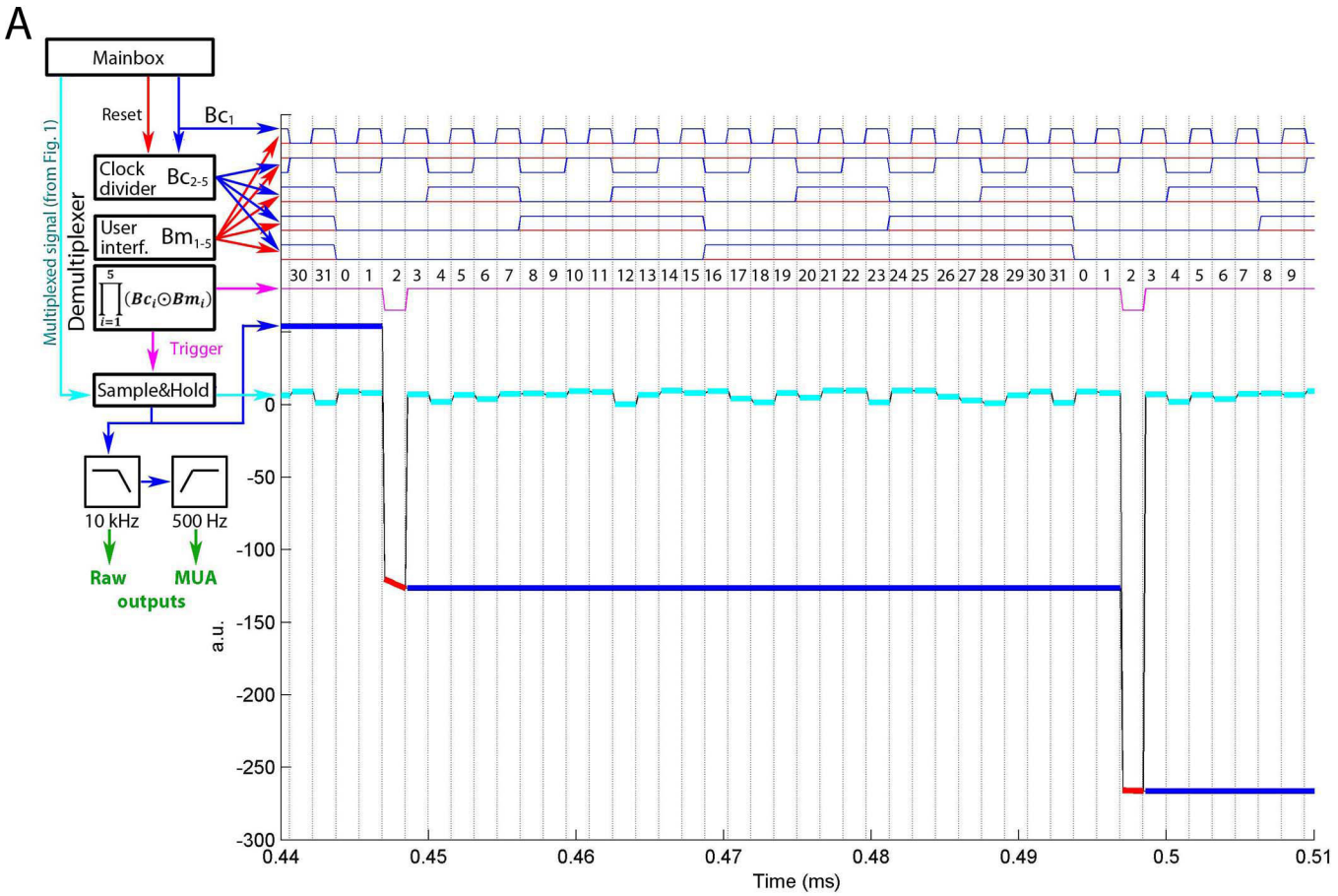


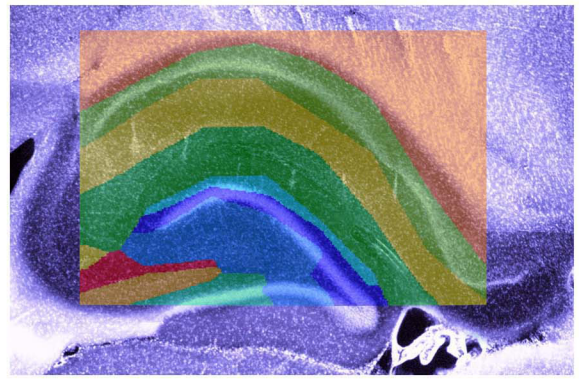
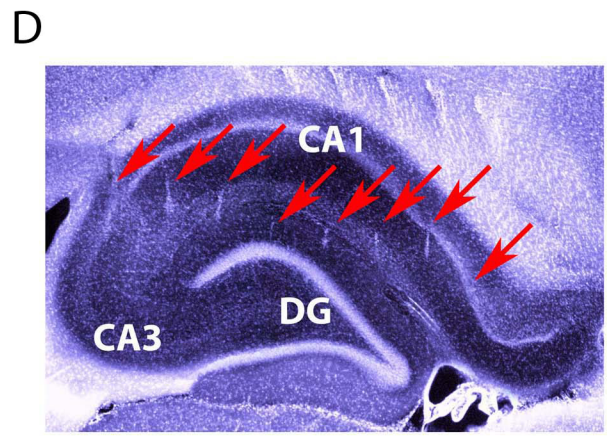
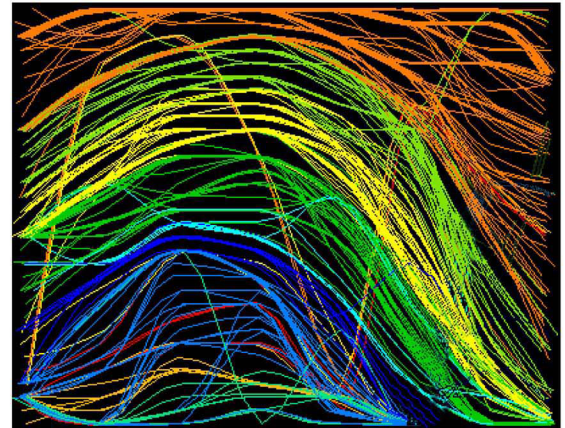
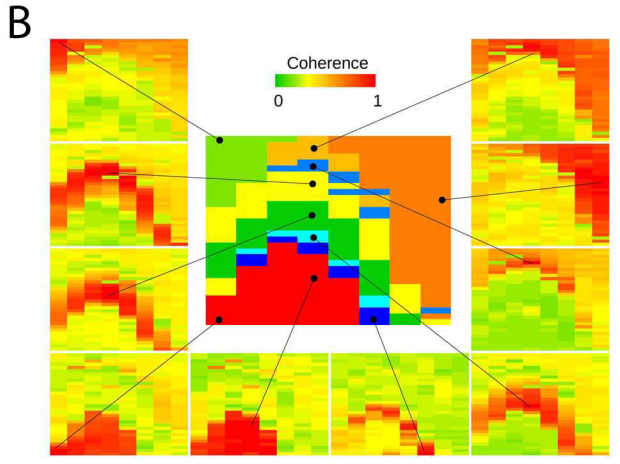
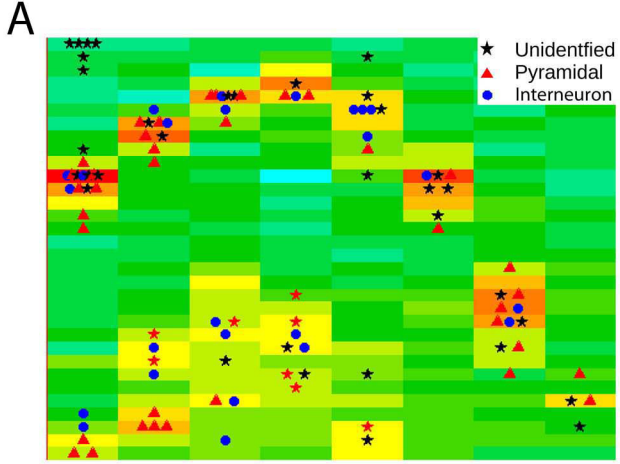
C 64-channel multiplexer with probe (top) (bottom)

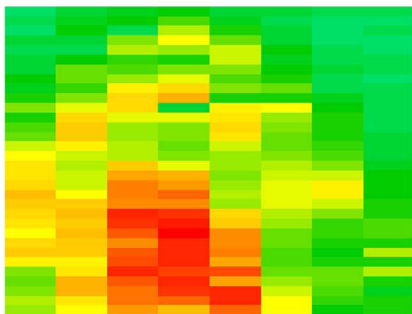


D Multiplexer circuit diagram



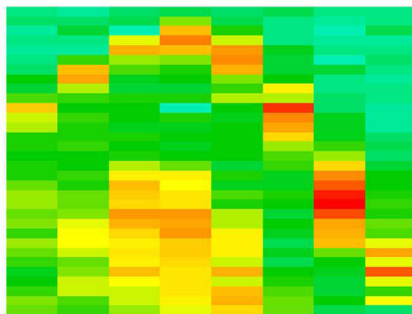






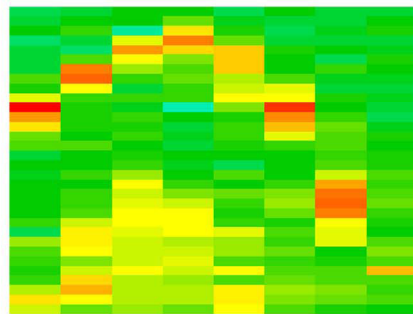
90 - 140 Hz

Min= 118 $\mu\text{V}/\sqrt{\text{Hz}}$; Max= 690 $\mu\text{V}/\sqrt{\text{Hz}}$



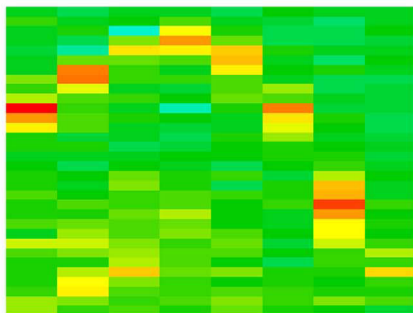
140 - 300 Hz

Min= 77 $\mu\text{V}/\sqrt{\text{Hz}}$; Max= 298 $\mu\text{V}/\sqrt{\text{Hz}}$



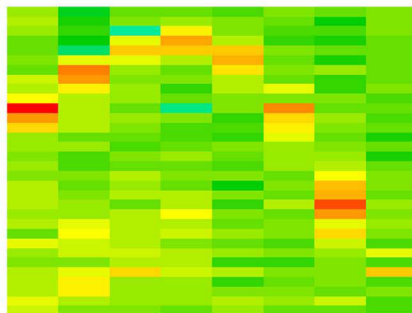
300 Hz

Min= 44 $\mu\text{V}/\sqrt{\text{Hz}}$; Max= 187 $\mu\text{V}/\sqrt{\text{Hz}}$



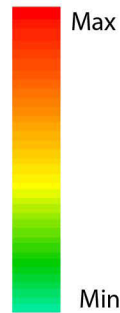
300 - 600 Hz

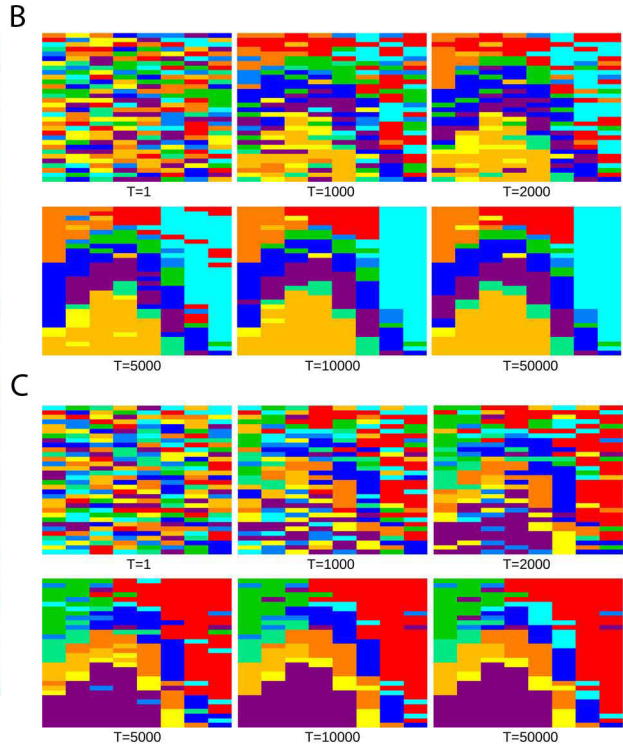
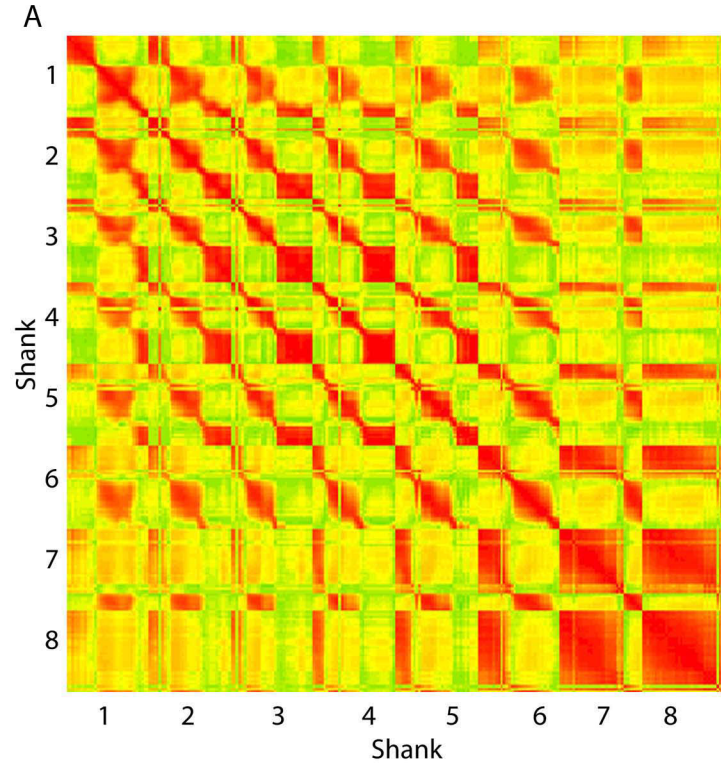
Min= 32 $\mu\text{V}/\sqrt{\text{Hz}}$; Max= 122 $\mu\text{V}/\sqrt{\text{Hz}}$

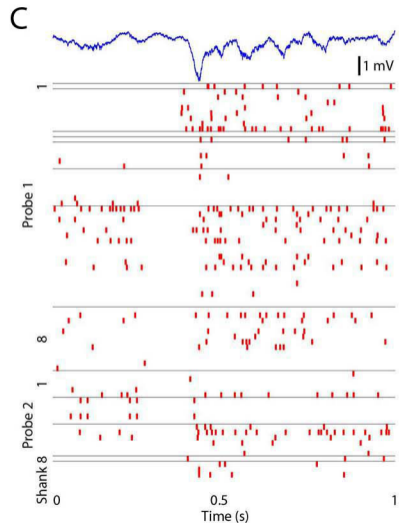
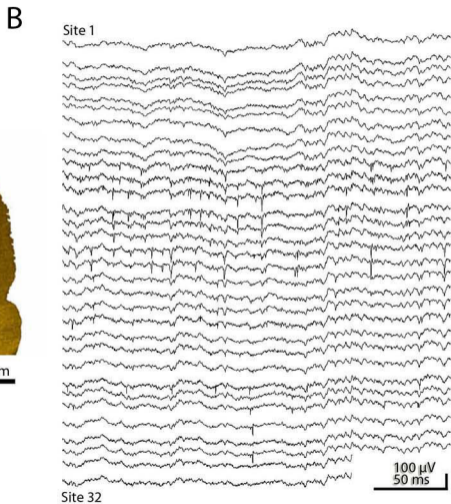
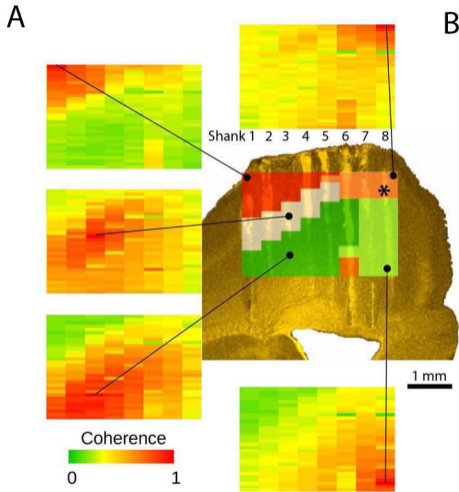


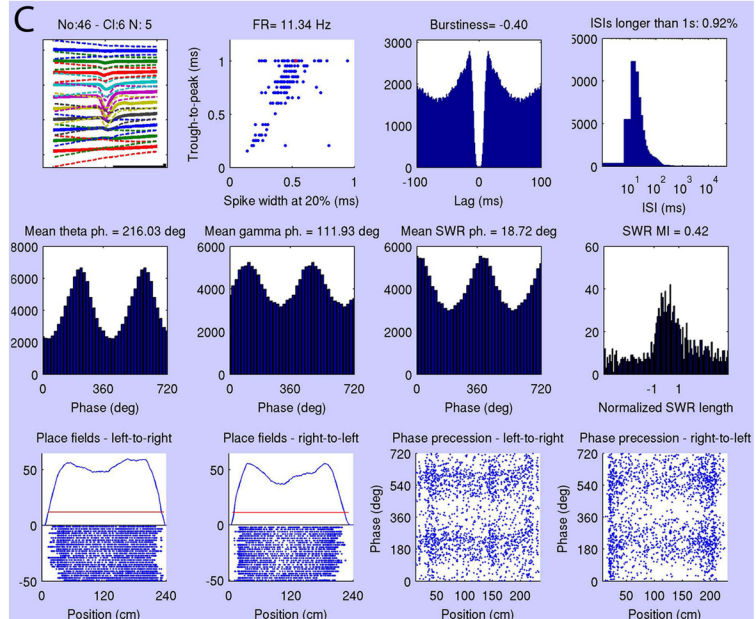
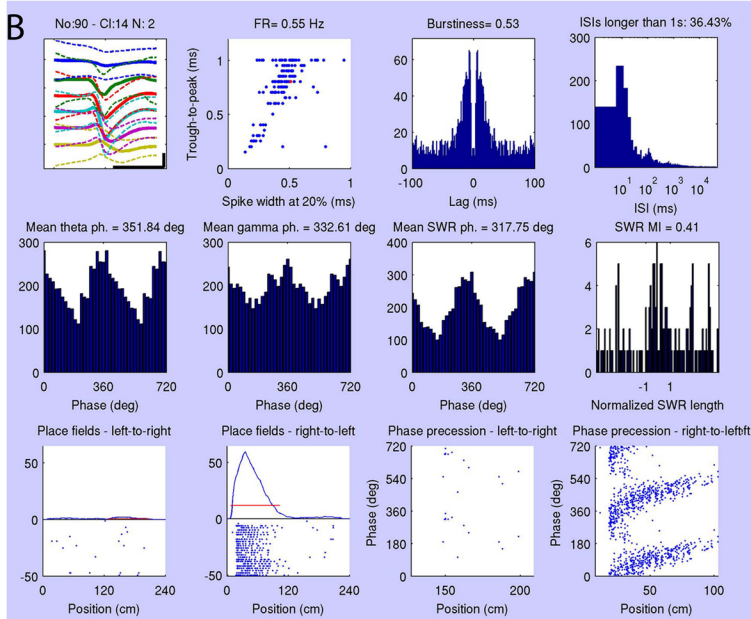
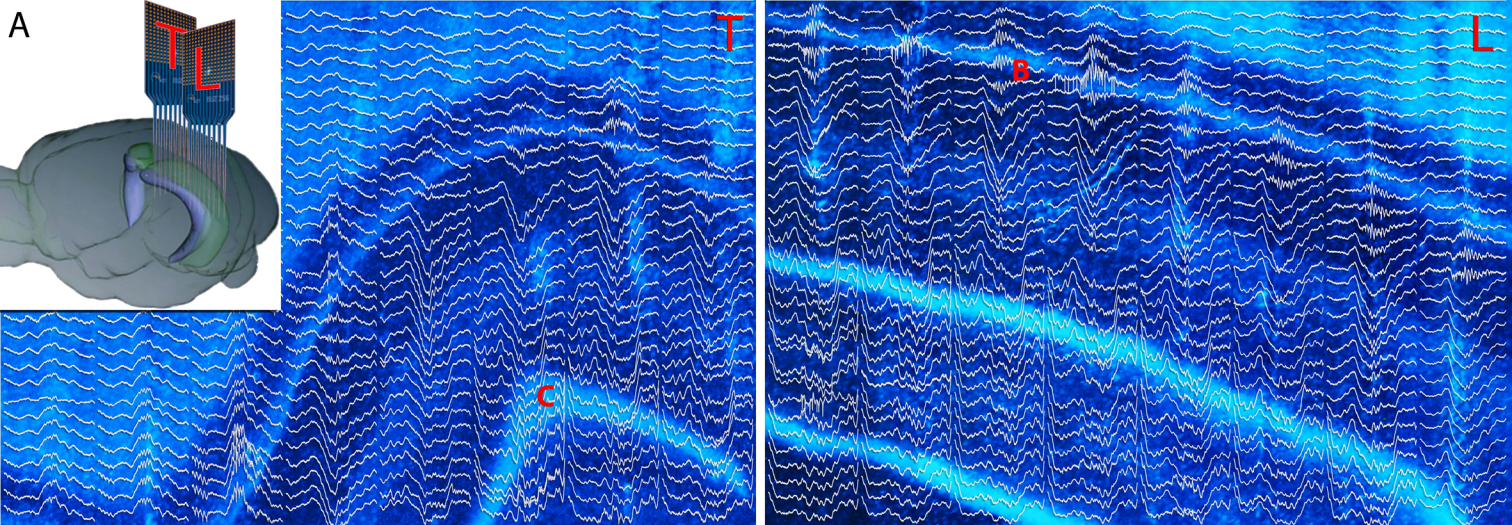
300 - 6000 Hz

Min= 8 $\mu\text{V}/\sqrt{\text{Hz}}$; Max= 41 $\mu\text{V}/\sqrt{\text{Hz}}$



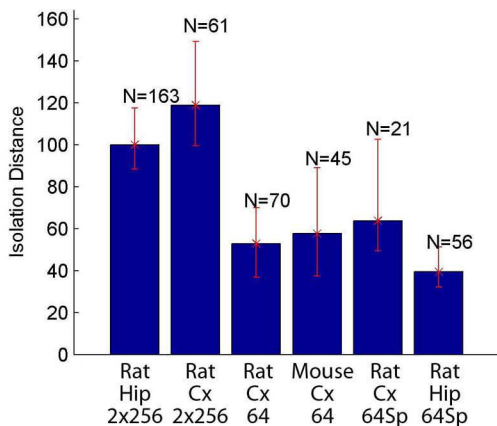




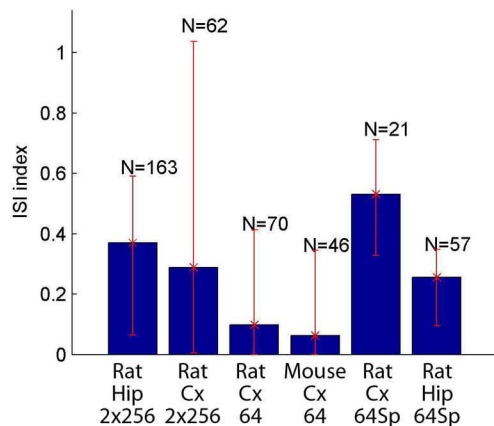


Permissive (ID>30 or ISIindex<0.4):

A

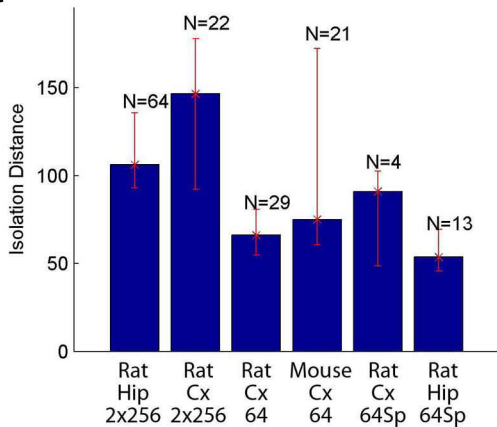


B

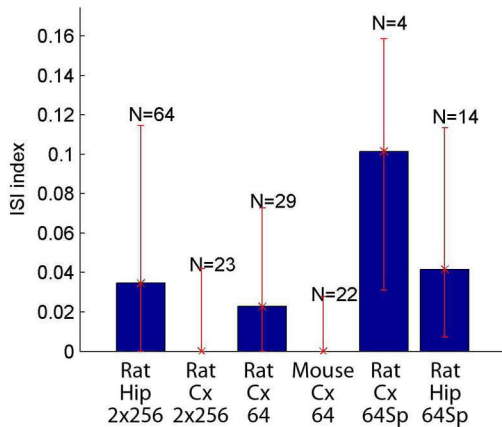


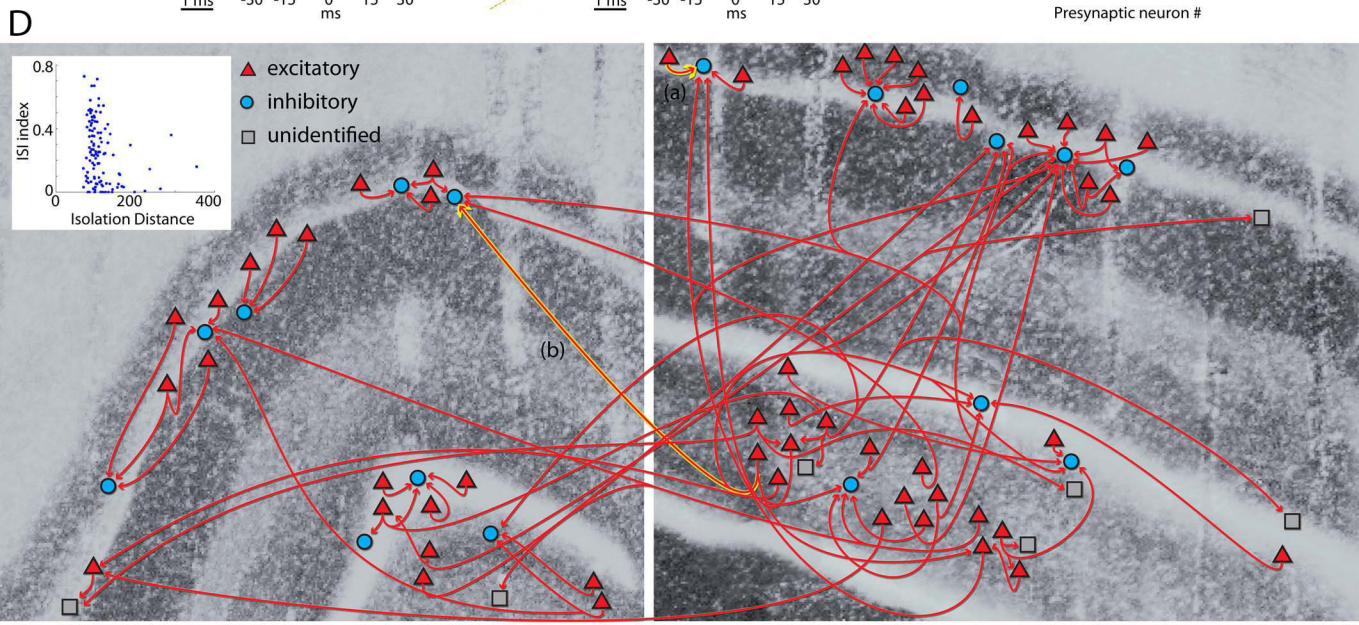
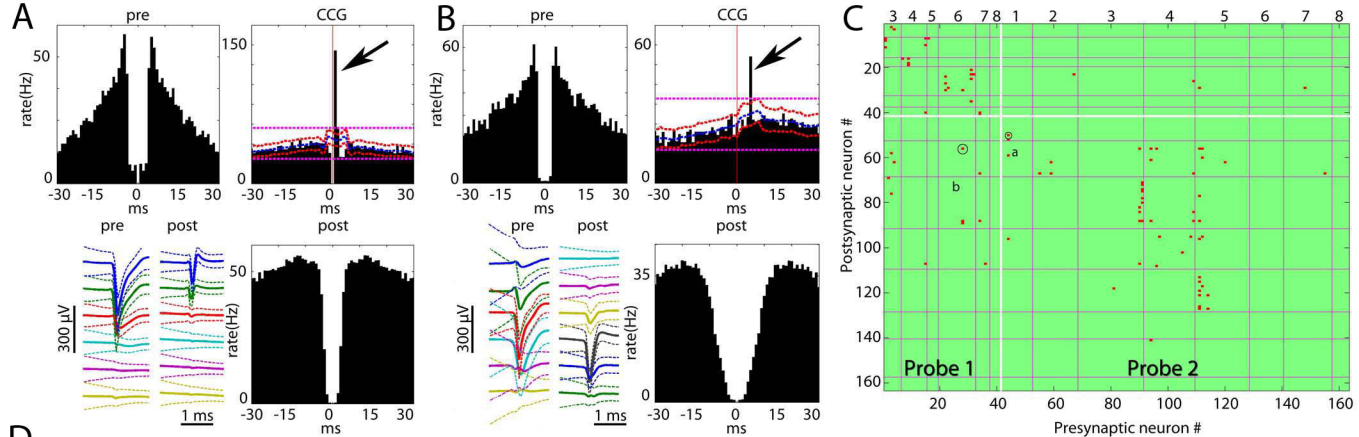
Conservative (ID>40 and ISIindex<0.2):

C



D





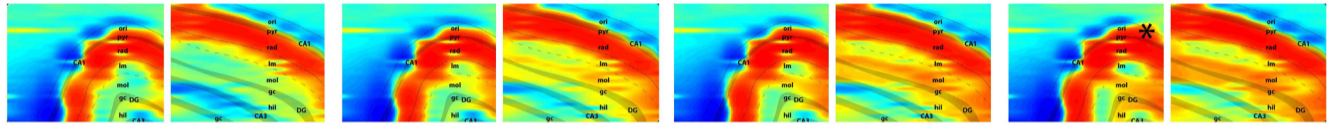
A SWR

-3 ms

-2 ms

-1 ms

0 ms



B Theta

